

Quasi-Equilibrium States in the Tropics Simulated by
a Cloud-Resolving Model. Part 1: Specific Features and Budget Analysis

C.-L. Shie, W.-K. Tao, J. Simpson, and C.-H. Sui

Popular Summary

Over the last two to three decades meteorologists have developed sophisticated cloud models (called Cloud Resolving Models) to study atmospheric convective systems. These models have increasingly been used in recent years to study the tropical region. Usually, the regional convective system, which is governed by the large-scale environmental conditions (such as the wind field, solar and infrared radiation, and sea surface temperature), reaches a balanced state in both heat (air temperature) and moisture (water vapor) within a certain period of time (e.g., several days to a few weeks). Using a locally developed cloud resolving model (Goddard Cumulus Ensemble Model), a series of long-term numerical experiments are performed that simulate the tropical convective system to examine the impact on the balanced states of convective systems under various environmental conditions.

The model results show that the genesis of a warm/wet balanced state is mainly due to either strong vertical wind shear or large evaporation from the ocean surface, while a cold/dry balanced state is attributed to weak wind shear along with small surface evaporation. In general, the moisture exchange at the ocean surface and the heat transport in the atmosphere by large-scale motions are the two dominant physical processes controlling the beginning stage of a convective system. They considerably weaken in the final stage, which leads to a balanced state. It is found that a system with a warmer/wetter state rains more than that with a colder/drier state, as convective clouds are the leading source of rainfall over stratiform clouds even though the former occupy much less area. Convective systems that consist of distinct cloud types due to the variation in horizontal winds are also found to propagate differently. The vertical structure of the heat budget, moisture budget, and cloud-scale motions as well as several other features such as atmospheric stability and circulation are also investigated and found to be significantly different between a warm/wet and cold/dry state. Detailed comparisons between the various states are presented.

Abstract

A series of long-term integrations using the two-dimensional Goddard Cumulus Ensemble (GCE) model were performed by altering imposed environmental components to produce various quasi-equilibrium thermodynamic states. Model results show that the genesis of a warm/wet quasi-equilibrium state is mainly due to either strong vertical wind shear (from nudging) or large surface fluxes (from strong surface winds), while a cold/dry quasi-equilibrium state is attributed to a remarkably weakened mixed-wind shear (from vertical mixing due to deep convection) along with weak surface winds. In general, latent heat flux and net large-scale temperature forcing, the two dominant physical processes, dominate in the beginning stage of the simulated convective systems, then considerably weaken in the final stage, which leads to quasi-equilibrium states.

A higher thermodynamic regime is found to produce a larger rainfall amount, as convective clouds are the leading source of rainfall over stratiform clouds even though the former occupy much less area. Moreover, convective clouds are more likely to occur in the presence of strong surface winds (latent heat flux), while stratiform clouds (especially the well-organized type) are favored in conditions with strong wind shear (large-scale forcing). The convective systems, which consist of distinct cloud types due to the variation in horizontal winds, are also found to propagate differently. Accordingly, convective systems with mixed-wind shear generally propagate in the direction of shear, while the system with strong (multidirectional) wind shear propagates in a more complex way. Based on the results from the temperature (Q1) and moisture (Q2) budgets, cloud-scale eddies are found to act as a hydrodynamic "vehicle" that cascades the heat and moisture vertically. Several other specific features such as atmospheric stability, CAPE, and mass fluxes are also investigated and found to be significantly different between diverse quasi-equilibrium states. Detailed comparisons between the various states are presented.

Quasi-Equilibrium States in the Tropics Simulated by
a Cloud-Resolving Model. Part 1: Specific Features and Budget Analysis

by

C.-L. Shie^{1,2}, W.-K. Tao², J. Simpson² and C.-H. Sui²

¹Goddard Earth Sciences and Technology Center
University of Maryland, Baltimore County
Baltimore, Maryland 21250

²Laboratory for Atmospheres
NASA/Goddard Space Flight Center
Greenbelt, Maryland 20771

J. of Climate

(October 29, 2001)

Corresponding author address: Dr. Chung-Lin Shie, Mesoscale Atmospheric Process
Branch, Code 912, NASA/GSFC, Greenbelt, MD 20771
e-mail: shie@agnes.gsfc.nasa.gov

1 Introduction

2 Model

2.1 Model setup

2.2 Experimental design

2.3 Budget equations

3 Modeled tropical quasi-equilibrium states

3.1 General features of modeled tropical quasi-equilibrium states

3.2 Specific characteristics of modeled tropical quasi-equilibrium states

3.2.1 Propagation of convective systems

3.2.2 Characteristics of rainfall (convective and stratiform)

3.2.3 Dry- and pseudo-adiabatic stabilities

3.2.4 CAPE and wet-bulb potential temperature

3.3 Heat, moisture and cloud mass budgets

3.3.1 Heat (Q1) and moisture (Q2) budgets

3.3.2 Mass fluxes

4 Thermodynamic Budget Analysis

4.1 Thermodynamic budget before and during quasi-equilibrium states

4.2 Impact on thermodynamic budget due to various horizontal wind structures

5 Summary

6 Acknowledgments

7 References

1. Introduction

Increasing attention has been given to cloud resolving models (CRMs or cloud ensemble models-CEMs) in recent years for their ability to simulate the radiative-convective system, which plays a significant role in determining the regional heat and moisture budgets in the tropics. The growing popularity of CRM usage can be credited to its inclusion of crucial and physically relatively realistic features such as explicit cloud-scale dynamics, sophisticated microphysical processes, and explicit cloud-radiation interaction (e.g., Islam et al. 1993, Held et al. 1993; Sui et al. 1994, Grabowski et al. 1996, and Tao et al. 1999, hereafter S94, G96 and T99, respectively; and others – see discussion and Table 1 in T99).

Several recent CRM studies show that certain model setups are critically responsible for some common model responses. These include three major aspects. First, how the large-scale forcing is prescribed -- time-invariant or time-varying observations or modeled large-scale advective forcing (e.g., Yamasaki 1975, Soong and Ogura 1980, Soong and Tao 1980, Tao and Soong 1986, Nakajima and Matsuno 1988, S94, G96, Xu and Randall 1996, T99, Li et al. 1999, and Xu and Randall 1999, hereafter XR99). Second, how the radiation is treated -- a fixed one-way radiation input or a two-way cloud-radiation interaction (e.g., Islam et al. 1993, Held et al. 1993, and Robe and Emanuel 1996). Third, how and what type of large-scale horizontal winds are applied – a weak wind shear due to time-varying vertical mixing, a strong wind shear maintained by almost time-invariant nudging, or simply no basic zonal flow (e.g., Held et al. 1993, S94, G96, T99, and Peng et al. 2001).

A few of the aforementioned research studies are briefly reviewed here. Employing interactive cloud-radiation processes and an assumed surface heat flux in balance with radiative cooling (i.e., no net heat allowed) in a three-dimensional cloud model, Islam et al. (1993) produced radiative-convective equilibrium states in the tropics. Using a two-dimensional cloud model with interactive cloud-radiation processes, Held et al. (1993) found that the model-generated rainband propagated in the direction of the low-level zonal mean winds; however, the precipitation system became “localized” (limited within a small portion of the domain) as zonal mean winds were removed. In a study with a two-dimensional cloud-radiation model, Randall et al. (1994) reviewed the so-called “radiative-convective oscillations” mechanism that was prevalent in radiative-convective systems. Accordingly, a cycle of radiative destabilization (in general, radiation generated

a cooling effect for the air aloft) succeeded by convective stabilization (convection, on the other hand, tended to dry the boundary layer as well as warm the air aloft) could form under the proper circumstances.

Two distinctive two-dimensional CRM simulations by S94 and G96, however, showed dramatically different quasi-equilibrium states regardless of model similarity and initial sounding data used (e.g., the imposing of an observed mean (time-invariant) vertical velocity). The former produced a colder/drier statistical quasi-equilibrium state than the latter. In an attempt to identify the plausible causes for such a drastic discrepancy between these two model results, T99 delved into the problem by performing a systematic series of numerical experiments simulating thermodynamic quasi-equilibrium states over a tropical ocean domain using the Goddard Cumulus Ensemble (GCE) model. In their findings, T99 suggested that the different treatment for horizontal wind shear applied in S94 (allowed vertically-mixing by deep convection that swiftly and greatly weakened an otherwise strong initial horizontal wind shear) and G96 (permitted the strong initial wind shear to be maintained almost time-invariant by geostrophy) was one of the two main factors that produced these two greatly diverse quasi-equilibrium states. Surface fluxes, which were computed with an imposed minimum surface wind, were found to be the other crucial factor in determining the tropical quasi-equilibrium states.

Overall, T99 focused their general discussion on large-scale mechanisms and the associated physical processes that accounted for the occurrence of various modeled quasi-equilibrium states, while many specific and detailed characteristics such as the cloud organization, the precipitation features and system propagation, and the cloud-scale eddy transport involved in the vertical distribution of heat (temperature) and moisture (water vapor) were not discussed. As a continuation of the study by T99, this paper serves four major objectives. First, the general features and the specific characteristics of convective systems (such as system propagation, convective and stratiform rainfall) associated with various quasi-equilibrium states will be examined. Second, the major characteristics associated with the atmospheric states (such as stability and CAPE) will be investigated. The third objective is to present a detailed analysis on the vertical structure of the heat, moisture, and Q1 and Q2 budgets as well as cloud mass fluxes. The final objective in this paper is to present the budget analysis for stages both before and during the quasi-equilibrium states.

The detailed model setup and the sensitivity experiments chosen for presentation are described in section 2. Section 3 presents the major findings and discussions on the modeled tropical quasi-equilibrium states, which is divided into three sub-sections. The first sub-section includes a presentation of general features for the diverse quasi-equilibrium states. The second presents a detailed discussion on the specific features and characteristics of the model simulations, while the third provides a detailed discussion (via vertical cross-sections) on the physical processes associated with both the heat and moisture budgets. Thermodynamic budget analyses which examine the genesis and maintenance of quasi-equilibrium states as well as the horizontal wind structure effects (wind shear and surface wind speed effects) are presented in section 4. A summary is concluded in section 5.

2. Model

2.1 *Model setup*

The GCE model is an anelastic, nonhydrostatic model that has been broadly used to study cloud-radiation interaction, cloud-environment interaction, and air-sea interaction. The cloud microphysics include a Kessler two-category liquid water scheme [cloud water and rain] and a three-category ice microphysics scheme [cloud ice, snow, and hail/graupel]. The model includes shortwave (solar) and longwave (infrared) radiative transfer processes, and a subgrid-scale turbulence scheme (one-and-a-half order TKE).

This model includes a stretched vertical coordinate of 31 grid points (with height increments from a 173-m resolution in the lower boundary layer to a 1057-m coarse resolution at the top) as well as a uniform horizontal coordinate with a cyclic boundary condition and a 1500-m resolution for a total of 512 grid points. A constant sea surface temperature of 28.18 °C is prescribed. A gustiness wind effect is considered by specifying a minimum surface wind speed in the bulk aerodynamic formulas. S94 assumed a 4 ms⁻¹ minimum surface wind, while one more wind value (1 ms⁻¹) was included in T99. In this study, a 7 ms⁻¹ minimum surface wind that is close to the surface wind in the nudging (strong wind shear) runs is also tested. All numerical runs are integrated for twenty-five days (reaching or near statistically quasi-equilibrium states).

2.2 *Experimental design*

There are six idealized numerical runs chosen for presentation in this paper. They involve various model setups pertaining to two major components: the vertical wind shear pattern and the minimum surface wind speed used for surface flux computation, which could be critical in determining the modeled quasi-equilibrium states (Table 1). The naming convention for these runs is explained in the table captions. For example, for run “4M” a minimum surface wind speed of 4 ms⁻¹ (“4”) in the bulk formulas and a mixed-wind shear condition (“M”) are applied. The zonal wind profile is vertically well mixed with time by deep convection (as in S94) for the mixed-wind shear runs, while it is relaxed to its initial value (strong wind shear) in the counterpart runs with nudging (“N”, similar to G96). Three levels of minimum surface wind speed (1, 4 and 7 ms⁻¹) are applied to test their effects on quasi-equilibrium state variation through the imposed (computed) surface fluxes. The pair of runs with 7 ms⁻¹ is performed to particularly test the sensitivity of modeled quasi-equilibrium states to an embedded surface wind speed close to that of the averaged surface wind in the nudging runs (i.e., 7-8 ms⁻¹). All the runs presented in this study used the S94 soundings.

2.3 Budget equations

Horizontal integration (average) of the equations for potential temperature (θ), and water vapor (q_v) over the model horizontal domain yields

$$C_p \frac{\partial \bar{T}}{\partial t} = \left(L_v (\bar{c} - \bar{e}) + L_s (\bar{d} - \bar{s}) + L_f (\bar{f} - \bar{m}) \right) - C_p \bar{\pi} \bar{w} \frac{\partial \bar{\theta}}{\partial z} - C_p \bar{\pi} \frac{1}{\bar{\rho}} \frac{\partial}{\partial z} \bar{\rho} \bar{w}' \bar{\theta}' + Q_R, \quad (1)$$

$$L_v \frac{\partial \bar{q}_v}{\partial t} = - \left(L_v (\bar{c} - \bar{e}) + L_s (\bar{d} - \bar{s}) \right) - L_v \bar{w} \frac{\partial \bar{q}_v}{\partial z} - L_v \frac{1}{\bar{\rho}} \frac{\partial}{\partial z} \bar{\rho} \bar{w}' \bar{q}_v' \quad (2)$$

where variables with an overbar are horizontally-mean quantities, and deviations from the means are denoted by a prime, while c , e , d , s , f and m are condensation, evaporation, deposition, sublimation, freezing, and melting, respectively. T is temperature, and $\bar{\pi} = (p / P_{oo})^{R / C_p}$ is the nondimensional pressure, where p is the dimensional pressure and P_{oo} the reference pressure taken to be 1000 mb. C_p is the specific heat of dry air at constant pressure, and R is the gas constant for dry air. $-\bar{w} \frac{\partial \bar{\theta}}{\partial z}$ and $-\bar{w} \frac{\partial \bar{q}_v}{\partial z}$ are the large-scale advective cooling and moistening forcing; \bar{w} is the

prescribed large-scale vertical velocity (constant with time); $\frac{\partial \bar{\theta}}{\partial z}$ and $\frac{\partial \bar{q}_v}{\partial z}$ are model mean vertical potential temperature and water vapor gradients (varying with time); $-\frac{1}{\bar{\rho}} \frac{\partial}{\partial z} \bar{\rho} \overline{w' \theta'}$ and $-\frac{1}{\bar{\rho}} \frac{\partial}{\partial z} \bar{\rho} \overline{w' q'_v}$ are the vertical eddy flux convergence/divergence for potential temperature and water vapor, respectively. Q_R is the radiative heating containing solar and infrared radiation. The variables L_v , L_f , and L_s are the latent heats of condensation, fusion and sublimation, respectively. The large-scale advective cooling/moistening forcing applied in the model is integrated using a time-varying gradient of modeled temperature/water vapor, along with a constant observed large-scale vertical velocity (similar to S94, G96 and T99). Note that the apparent heat source Q_1 and the apparent moisture sink Q_2 (e.g., Yanai et al. 1973) can be readily defined using equations (1) and (2), respectively,

$$Q_1 \equiv \left(L_v (\bar{c} - \bar{e}) + L_s (\bar{d} - \bar{s}) + L_f (\bar{f} - \bar{m}) \right) - C_p \bar{\pi} \frac{1}{\bar{\rho}} \frac{\partial}{\partial z} \bar{\rho} \overline{w' \theta'} + Q_R, \quad (3)$$

$$Q_2 \equiv - \left(L_v (\bar{c} - \bar{e}) + L_s (\bar{d} - \bar{s}) \right) - L_v \frac{1}{\bar{\rho}} \frac{\partial}{\partial z} \bar{\rho} \overline{w' q'_v}. \quad (4)$$

3. Modeled tropical quasi-equilibrium states

In this section, general features of the quasi-equilibrium states of temperature and water vapor for the six runs are first discussed. Then, several specific features, such as rainband propagation, rainfall properties, dry- and pseudo-adiabatic stabilities, and CAPE associated with various quasi-equilibrium states in the radiative-convective system are presented. Finally, vertical distributions of the heat and moisture budgets as well as mass fluxes are examined for different quasi-equilibrium states.

3.1 General features of modeled tropical quasi-equilibrium states

A scatter plot of domain-averaged water vapor versus temperature at their quasi-equilibrium states (25 days of integration) for the six runs listed in Table 1, along with the results of S94 (“S”) and G96 (“G”) is shown in Fig. 1. Three distinct thermodynamic regimes (shown by the three boxes) are characterized as follows: (1) warm/wet with T and q_v above 261.8°K and 67.0 mm, respectively, (2) mild/moist with T between 259.5°K and 260.0°K, and q_v between 57.5 mm and 60.0 mm, (3) cold/dry with T

and q_v below 256.5°K and 48.1 mm. Note that the mild/moist and cold/dry regimes (each includes only one numerical experiment) are categorized based on results also from several other numerical experiments that are not presented in this paper (those will be presented in a future Part 2 paper).

Two major characteristics can be generalized from Fig. 1. First, the strong wind shear and surface wind due to nudging have a prominent impact on quasi-equilibrium state variation for runs with lower minimum wind speeds. For runs with 1 ms^{-1} , this prominent effect lifts the mixed-wind shear run 1M from a cold/dry regime up to 1N a warm/wet regime (up by two regimes). However, for runs with a moderate minimum surface wind of 4 ms^{-1} , 4N in the warm/wet regime is only one regime above 4M of the mild/moist regime. For the pair of runs with the highest minimum wind speed 7 ms^{-1} , 7N is relatively warmer/wetter than 7M, but they are classified within the same warm/wet regime. The impact due to strong wind shear substantially diminishes as the prescribed minimum wind speed increases toward the magnitude of surface wind speed found in the strong wind shear runs (i.e., $7\text{-}8 \text{ ms}^{-1}$). This prominent nudging effect that accounts for a significant contribution in both temperature and water vapor comes by way of two primary processes – first, a greater large-scale forcing process due to the strong vertical wind shear, and second, a greater surface flux process owing to a relative surge of surface wind speed by the wind shear. Later budget analyses clearly show that the impact by nudging peaks for the 1 ms^{-1} runs when both processes genuinely contribute, whereas it greatly weakens for the 7 ms^{-1} runs when the contribution by the surface flux process becomes much weaker.

Second, the imposed minimum surface wind for computing surface fluxes also plays a crucial role in determining the quasi-equilibrium state, particularly for runs with a mixed-wind shear where surface winds are very weak (about $1\text{-}2 \text{ ms}^{-1}$, see Fig. 2 shown later). In Fig. 1, the three mixed-wind shear runs are spread over the three thermodynamic regimes depending on the respective minimum winds, while the three strong wind shear (nudging) runs all reside in the warm/wet regime. For mixed-wind shear runs, a higher minimum surface wind produces a larger surface flux into the atmosphere, which accounts for a quasi-equilibrium state upgrade. On the other hand, the high surface wind speed in all strong wind shear runs minimizes the impact of the minimum surface wind on quasi-equilibrium state variation.

It can be concluded that a warm/wet regime is either due to strong vertical wind shear (from nudging) or/and strong surface fluxes (from strong surface winds), while a cold/dry regime is attributed to a notably weakened wind shear (from vertical mixing) along with weak surface winds. Fig. 2 shows two sets of 5-day averaged wind shear profiles for a pair of runs 4M (mild/moist) with mixed-wind shear, and 4N (warm/wet) with strong wind shear, respectively. The horizontal wind shear is greatly weakened (vertically all light west winds except at the very top for the final five days) in 4M due to the strong vertical-mixing process by deep convection. On the other hand in 4N, a strong horizontal wind shear with easterly flow below and westerly aloft has been maintained (almost time-invariant) due to the nudging process.

3.2 Specific characteristics of modeled tropical quasi-equilibrium states

3.2.1 Propagation of convective systems

The strong wind shear due to nudging favors the generation of well-organized cloud systems with large stratiform clouds. The induced surface wind surge also increases the amount of erect, yet non-precipitating convective clouds (discussed later). On the other hand, surface fluxes (due to minimum surface wind) enhance erect precipitating convective clouds in the mixed-wind shear runs. The diverse cloud systems generated by the mixed-wind shear and strong wind shear runs also propagate differently. Most likely the diverse large-scale wind shear structures (e.g., in 4M and 4N) are the key elements. Surface rainrate data for 4M and 4N are shown in a time-distance diagram for the final five days in Figs. 3a and 3b, respectively. Rainbands in 4M are mainly associated with sporadic precipitating clouds dominated by convective cells and unorganized stratiform clouds, and move eastward with an estimated phase speed slightly greater than 2 ms^{-1} ($\sim 7.7 \text{ km hr}^{-1}$). The strong wind shear run 4N possesses a dramatically different rainband system and the way it migrates. The much broader rainbands mainly associated with massive stratiform cloud clusters seem to form at certain favored locations and migrate eastward with a phase speed around 10.7 ms^{-1} ($\sim 38.6 \text{ km hr}^{-1}$) before they dissipate, whereas the sparse and small rain spots relevant to the erect but relatively shallow convective cells propagate westward with a phase speed of about 8.7 ms^{-1} ($\sim 31.4 \text{ km hr}^{-1}$).

The eastward (about 2 ms^{-1}) propagating rainband systems (mainly the shallow and deep convective cells) in 4M are driven by a light net westerly steering effect due to

light west winds at all levels (an average of 1.71 m/s and a surface value of 1.68 m/s) except at the very top (see Fig. 2). In contrast, the more complex propagating systems in 4N are attributed to a more complicated wind shear due to nudging, which possesses strong easterly flow below 580 mb (around 5 km in height) and strong westerly above it (also see Fig. 2). With the rainband systems of 4N, the shallow convective clouds propagate westward mainly due to the easterlies prevailing in the lower atmosphere, while the eastward-moving well-organized stratiform clouds are promoted by excited gravity waves that move eastward in a duct under the westerlies aloft. The eastward-moving well-organized cloud system however dissipates after indefinite periods of time (usually a couple of hours).

In a recent study using a two-dimensional cloud model, Shige and Satomura (2001) suggested that gravity waves (disturbances) excited by the mesoscale cloud line played a crucial role in the sequential generation of new convective bands to the west of an old eastward-moving convective band with a prescribed wind shear of west winds at low levels and strong easterlies aloft. The excited disturbances propagated westward in a wave duct in the troposphere that was formed by the easterlies aloft. The nudging shear pattern in our study is quantitatively similar to that of Shige and Satomura (2001) except for wind directions being reversed; therefore, a similar rainband propagation type is found in both studies. Moreover, Held et al. (1993) found that rainbands in convective systems propagated in the direction of the low-level mean zonal winds, which was attributed to the uni-direction of the vertical wind shear. It may be concluded that the large-scale zonal wind shear plays a crucial role in determining the formation as well as the migration of the radiative-convective system not only by its wind intensity and vertical gradient, but also by the wind direction that it veers with height.

Fig. 4a shows erect convective clouds that develop in a mixed-wind shear environment (4M of mild/moist), while Fig. 4b displays a well-established stratiform cloud cluster prevailing in a strong wind shear scenario (4N of warm/wet). By tracing the wind vectors, circulation cells may be approximated for these two cases. In 4M, a relatively short clockwise-circulation cell (centered around 250-260 km and 700-750 mb) located east (ahead) of the major erect cloud plus a relatively tall counterclockwise-circulation cell (centered around 180-190 km and 450-500 mb) west of (behind) it, are primarily triggered by convergence associated with deep convection. On the other hand, in 4N, a horizontally-elongated and vertically-flattened “conceptual” circulation cell (centered around 300-310 km and 600-620 mb at the base of the anvil) can be roughly

drawn within the well-organized cloud cluster and is mainly induced by the strong wind shear. Note that the regular stratiform clouds (the unorganized type partitioned out of the convective clouds) still dominate in coverage (to be discussed later) in the mixed-wind shear runs; however, the strong wind shear (Fig. 2) further enhances the stratiform cloud coverage by generating extensive well-organized stratiform clouds (Fig. 4b). Details for how the “stratiform” and “convective” clouds are defined (partitioned) can be found in Tao et al. 1993, and S94.

3.2.2 Characteristics of rainfall (convective and stratiform)

A scatter diagram of the 25-day surface rainfall (in mm) versus the rainfall contribution by stratiform clouds (in percentage) for the six runs is shown in Fig. 5a. It shows that the warm/wet runs (1N, 4N, 7N, and 7M) generally produce larger rainfall than the colder/drier runs (4M and 1M), while the respective contributions by convective and stratiform clouds vary depending on the vertical structure of the horizontal winds. Among warm/wet runs, those associated with strong wind shear (1N, 4N, and 7N) favor higher stratiform rainfall percentages (between 41 and 44%), while the sole mixed-wind shear run 7M favors less rainfall contribution by stratiform clouds (31.5 %). Among mixed-wind shear runs (1M, 4M, and 7M), the contribution by convective/stratiform clouds quasi-linearly increases/decreases with enhanced rainfall as the minimum surface wind increases. They imply that, for runs with weak wind shear, the larger surface fluxes generate more convective clouds responsible for the increased rainfall, while for runs with strong wind shear, the enhancement in precipitation mainly comes from the (well-organized) stratiform clouds. Overall, convective clouds (between 56 and 70%) dominate over stratiform clouds (between 30 and 44%) in rainfall contribution. Based on a series of earlier studies (e.g., Houze 1977; Cheng and Houze 1979; Gamache and Houze 1983), stratiform clouds were often found responsible for around 40% of precipitation in tropical convective systems.

Fig. 5b shows that the cloud area coverage for warm/wet runs with strong wind shear (1N, 4N, and 7N) is significantly larger in both stratiform and convective clouds than mixed-wind shear runs (1M, 4M, and 7M), particularly in stratiform clouds. The strong wind shear intensifies the total cloud area coverage by providing the convective system, first with an environment favorable for the enhancement of large-scale forcing that produces well-organized clouds, and second with a strong surface wind that strengthens the surface fluxes which generates more convective clouds. On the other

hand for runs with low (mixed-wind) wind shear, the enhancement in surface fluxes due to the increased minimum surface wind only tends to extend/reduce the cloud coverage in convective/stratiform clouds; however, the total cloud coverage remains unchanged. Nonetheless, an increase in total cloud coverage in warm/wet runs with strong wind shear does not guarantee a substantial increase in total rainfall production (compare 1N with 4N, or 7N with 7M in Fig. 5a and Fig. 5b). This feature will be further discussed later. Moreover, stratiform clouds are more extensive than convective clouds (particularly for the warm/wet runs with strong wind shear) even though they produce relatively less precipitation.

Rainfall histograms of rainfall amount and rainfall frequency were constructed for all six runs to analyze different rainfall distributions for various quasi-equilibrium states. The results generally show two different types of pattern, which mainly depend on the wind shear patterns, i.e., strong wind shear or mixed-wind shear. Therefore, results presented in Fig. 6 only include one pair of runs – the warm/wet run 4N with strong wind shear and the mild/moist run 4M with mixed-wind shear. Histograms shown are averages of instantaneous rainrate histograms over the 25-day period. The upper two panels are histograms for surface rainfall amount, while the lower two panels are the associated histograms for surface rainfall frequency (occurrence), which are normalized by their total occurrence and expressed in percentage. Overall, the lightest rainrate ($0 - 2 \text{ mm hr}^{-1} \text{ grid}^{-1}$) dominates in both amount and frequency for the warm/wet run with strong wind shear, while the second lightest rainrate $2 - 4 \text{ mm hr}^{-1} \text{ grid}^{-1}$ accounts for the peak amount for the mild/moist run with mixed-wind shear. The lightest rainrate maintains its dominance in frequency for the mild/moist run, yet it is not as vital as it is for the warm/wet run. The enhanced rainfall contribution by light-precipitating clouds due to strong wind shear comes mainly from the increased stratiform clouds [see following discussion]. Namely, the also enlarged convective cloud coverage due to strong wind shear does not contribute significant precipitation.

Based on the time-averaged domain rainfall results from the six runs, Table 2 lists both amount and frequency for two rainrate ranges – one of light precipitating rates (less than $4 \text{ mm hr}^{-1} \text{ grid}^{-1}$) and the other of strong precipitating rates (at least $24 \text{ mm hr}^{-1} \text{ grid}^{-1}$). Table 2 reveals a general feature that the strong wind shear runs dominate the mixed-wind shear runs in the light rainrate range for both amount and frequency, while the latter runs dominate the former ones for the strong rainrate range. In the light rainrate range, both rainfall amount percentage (%) and frequency are found positively

correlated to minimum surface wind for strong wind shear runs. An earlier finding (based on Fig. 5b) shows that stratiform cloud coverage increases in strong wind shear runs with increased minimum surface wind speed. They imply that the enlarged stratiform cloud coverage due to strong wind shear is responsible for the increased rainfall generated by light-precipitating clouds. The enhanced rainfall amount and frequency in the strong rainrate range as well as the increased convective cloud coverage (Fig. 5b) due to increased minimum wind speed for mixed-wind shear runs suggest the additional convective clouds are accountable for the enhanced rainfall generated with higher rainrates. On the other hand, the slightly increased convective cloud coverage with increased minimum surface wind due to strong wind shear (Fig. 5b) is found to be either non-precipitating or light-precipitating since both the rainfall amount (%) and frequency of high rainrates decrease as the minimum surface wind speed increases. The large amount of rainfall produced by the occasional (small frequency percentage) high rainrates associated with intense convective clouds (particularly for the mixed-wind shear runs) indicates why the convective clouds are the primary source for precipitation.

Precipitation efficiency for the six runs has also been examined by defining the total precipitation efficiency as the ratio of the total rainfall to the total condensation. The results show that total precipitation efficiencies range from 50% to 53% for mixed-wind shear runs to 41% to 42% for strong wind shear runs, which indicates that the upright convective clouds possess higher precipitation efficiencies than the well-organized tilted stratiform clouds. Apparently, the higher precipitation efficiency for convective clouds is crucial for their larger precipitation contribution. Our results qualitatively agree with the precipitation efficiencies found by Ferrier et al. (1996), i.e., 40% to 50% for the upright convection runs (erect storms) and 20% to 35% for the upshear-tilt runs.

3.2.3 *Dry- and pseudo-adiabatic stabilities*

Fig. 7a (Fig. 7b) shows a scatter diagram of the final 5-day averaged surface relative humidity versus lower-tropospheric (below the 4.3-km level) lapse rate of temperature (equivalent potential temperature) for the six runs (note that two extra values cM and cW from XR99 are also included in Fig. 7a). Equivalent potential temperature θ_e (950 mb) is generally found to increase in the troposphere (about 15 to 17 km deep from cold/dry to warm/wet runs) in the warm/wet runs relative to the colder/drier runs, especially in the lower atmosphere below the freezing level (~4 km near cloud base) and above the surface boundary layer. As a result, the warmer and more saturated

lower atmosphere (also deeper) found in the warm/wet runs possesses a stronger vertical gradient of θ_e (decreasing with height) compared to the colder/drier runs with a relatively colder and drier lower atmosphere. Figs. 7a – 7b clearly show that the lapse rate of temperature has a negative and linear correlation with relative humidity (or equilibrium states), while the lapse rate of equivalent potential temperature possesses a positive and linear correlation with relative humidity. Namely, the colder/drier runs (with weak wind shear and surface fluxes) reach a quasi-equilibrium state with a lower atmosphere that is more static-unstable (dry-adiabatic), while the warm/wet runs (with strong wind shear or strong surface fluxes) reach a state that is more moist-unstable (pseudo-adiabatic) in the lower atmosphere. Apparently, moisture (from latent heat flux or large-scale forcing) plays a crucial role in modifying the atmospheric stability. The aforementioned positive/negative linear relationships particularly found among mixed-wind shear runs (1M, 4M and 7M) again imply the direct and important role surface fluxes play in determining the quasi-equilibrium system.

The stability issue addressed here involves two perspectives: the moist-adiabatic (pseudo-adiabatic) and dry-adiabatic, especially considering that the former is commonly referenced in areas of tropical convection. The current results show that a final warmer (colder) and more humid (drier) quasi-equilibrium state tends to equilibrate with a more moist-unstable (thermal-unstable) lower atmosphere, which is equivalent to the statement by Tao et al. (2001): “The results shown in Fig. 2b indicate that the thermodynamic state is more unstable (stable) for those experiments that produced a warmer and more humid (cold and dry) SE state”. Williams and Renno (1993) indicated that more than half of the area in the tropical belt is conditionally pseudo-adiabatic unstable, even though the convective area is only a small fraction of the unstable area (which is also found in this study, see Fig. 5b). In a recent study, XR99 addressed the stability issue for tropical convective systems from the point of view of a dry-adiabatic environment [see their Figure 10b, and cM and cW are included in Fig. 7a here] by showing that the atmosphere was more thermally stable (unstable) for the warm/wet (cold/dry) thermodynamic regime.

3.2.4 CAPE and wet-bulb potential temperature

Additional thermodynamic quantities of the atmospheric state are also studied. We first examined the “soundings” near the end of the simulation time that were drawn on a pseudo-adiabatic chart using horizontally-averaged temperature and water vapor fields

(not shown). As expected, soundings of the warm/wet runs (either with strong wind shear or strong surface fluxes) are found warmer and more humid in a deeper moist lower atmosphere (up from around 630 mb to 560 mb) than those of the colder/drier runs (with weak wind shear and weak surface flux).

A moistened lower atmosphere is also apparent in the warm/wet regimes based on the scatter plot of CAPE versus θ_w in the surface layer for the six runs (Fig. 8). Both CAPE and θ_w are larger in the warm/wet runs than in the colder/drier runs, which again implies a positive correlation between a more pseudo-adiabatic unstable (stable) environment and the warm/wet (colder/drier) runs. Using the GISS GCM, Ye et al. (1998) produced a linear relationship between CAPE and θ_w in the surface layer and suggested the CAPE change was mostly determined by moisture variations in the boundary layer over the tropical ocean (part of their results are approximated and shown in Fig. 8). A few more features can be addressed from Fig. 8. First, the process of latent heat flux intensifies CAPE slower among mixed-wind shear runs (i.e., a less steep linear slope of CAPE- θ_w) than the process of large-scale forcing (due to strong wind shear) that enhances CAPE (steeper slopes). The mild/moist run 4M seems to be the more realistic simulation for its being in the linear trend of Ye et al. (1998), while the CAPE- θ_w correlation among the warm/wet runs is qualitatively similar to that of Ye et al. (1998) with quasi-parallel slopes.

3.3 Heat, moisture and cloud mass budgets

3.3.1 Heat (Q1) and moisture (Q2) budgets

Vertical profiles of individual time-mean (for the final 5 days representing the quasi-equilibrium state) and horizontally averaged temperature (water vapor) budget components are shown in Fig. 9a (Fig. 9c) for the mild/moist run 4M, and Fig. 9b (Fig. 9d) for the warm/wet run 4N. For the heat budget (Fig. 9a), the eddy heat flux term due to cloud-scale motion and sub-grid turbulence is coupled with the net sum of the other forcing terms (large-scale forcing, net condensation, and radiation). The two heating maxima in eddy heat convergence located near 4.8 km and 12.6 km, respectively, correspond with different heat budget balances though. The former responds to the combined heat loss associated with stronger cooling by large-scale forcing and a reduction in net condensational heating due to melting near the melting level (~ 4-5 km) and the latter to the sole strong radiative cooling near the top of deep clouds. At high

altitudes where both the large-scale forcing and cloud microphysical processes are no longer vital, the eddy transport becomes the prominent process that offsets the net radiation and maintains a balanced heat budget. The two regions with maximum net condensational heating above and below the melting level are compensated by large eddy heat divergence. In the boundary layer, eddy heat divergence compensates most of a net heat surplus consisting of heating from surface sensible heat flux and evaporative cooling due to falling precipitation. The results indicate that cloud-scale eddies act as a baroclinic “vehicle” that cascades heat down gradient by transferring heat from regions of surplus into regions of deficit by means of upward and downward convective motion. Note that the surface value of EFCt shown in the figure is actually a net heating by adding surface sensible heat flux (heating) to the lowest-level eddy heat divergence (cooling).

In 4N (Fig. 9b), both the heating due to net large-scale forcing and the cooling due to net radiation increase in both magnitude and vertical scale due to strong wind shear. However, the increase in temperature tendency (not shown) from 4M to 4N is mainly due to the enhanced net large-scale forcing process (most occurred below around 14 km). The eddy heat flux responds by expanding in the vertical with magnitudes slightly increased. Meanwhile, the region with a temperature tendency of cooling found in the upper atmosphere (above the top of deep clouds, not shown) shifts upward since the maximum eddy heat divergence occurs at higher levels where the longwave radiative heating peaks. This local radiative maximum is mainly attributed to strong longwave radiation emitted from the atmosphere below (deeper well-organized clouds with higher cloud ceilings), along with weak shortwave radiation.

Two layers of strong eddy moisture convergence are found around 4.2 km (4.8 km) and 9.2 km (9.6 km) for 4M in Fig. 9c (4N in Fig. 9d). These eddy moisture maxima nearly compensate the comparable net drying mainly due to microphysical processes involving vapor condensation and subsequent rain sedimentation in the lower atmosphere, and ice deposition/riming and sedimentation in the higher atmosphere. Similar to the heat budget, the grid-scale eddies play a similar role in vertically redistributing the water vapor field by cascading it down gradient. Some differences are however found between the heat and moisture budget distributions. Unlike the extensive vertical region of heat activity that goes beyond the cloud levels, the vertical region of moisture activity is primarily confined to cloud levels. Similar to the heat budget, the net large-scale forcing process intensifies the moisture contribution in both

magnitude and vertical scale in 4N; however, the large-scale forcing in moisture intensifies both above and below 4.5 km while the large-scale forcing in temperature is only enhanced in the upper atmosphere (above 4.5 km).

The vertical distribution of the apparent heat source $Q1$ and moisture sink $Q2$ are shown in Figs. 9e and 9f ($Q2$ is defined positive for a moisture sink). Vertical distributions of the $Q1$ budget qualitatively resemble those of net condensation heating Ct (Figs. 9a and 9b) for both 4M and 4N due to its dominance over the eddy heat flux convergence/divergence and net radiation. Overall, the $Q1$ budget is enhanced by strong wind shear; however, the level of maximum $Q1$ is determined by the local maximum in eddy heat convergence in the lower atmosphere (around 4.8 km for 4M and 5.3 km for 4N), which overcomes strong cooling by large-scale forcing and a heat loss in net condensation due to melting. On the other hand, a dual-peak distribution occurs in the $Q2$ budget as a considerable amount of moistening due to a maximum in eddy moisture convergence (around 4.2 km for 4M and 4.8 km for 4N) significantly compensates for a maximum drying in net condensation due to rain processes and forms a local minimum in drying. The strong wind shear raises the vertical level of maximum $Q2$ and intensifies the drying especially for the lower maximum. The eddy flux convergence/divergence terms re-shape the vertical distribution for both $Q1$ and $Q2$ by cascading heat and moisture vertically. Eventually, the vertical distributions of $Q1$ and $Q2$ resemble those of large-scale forcing in temperature and moisture, respectively, as the quasi-equilibrium state is reached with negligible temperature and moisture tendency (see Figs 9a – 9f).

3.3.2 Mass Fluxes

The evolved circulation of various convective systems can be exhibited by the mass fluxes. Fig.10 shows the vertical profiles of horizontally averaged mass fluxes for the mild/moist run 4M and warm/wet run 4N at their early and final stages. The two-peaks of the imposed total mass fluxes around 8.9 and 2.5 km critically affect the level of peak large-scale temperature forcing (see Figs. 9a & 9b) and the lower level peak in large-scale moisture forcing (see Figs. 9c & 9d). In general, positive net mass fluxes dominate in the convective cloud region, especially in the lower atmosphere, while positive/negative net mass fluxes prevail in the upper/lower atmosphere in the stratiform cloud region. However, positive net convective mass fluxes are stronger in the beginning stage, while net stratiform mass fluxes are enhanced (more positive aloft

and less negative below) in the final stage. Though the total mass fluxes are time-invariant, the respective upward and downward fluxes do vary with time (not shown). Upward and downward fluxes are much larger in the first five days compared to the final five days, and both fluxes are enhanced in 4N. The stronger initial circulation may be caused by the spurious energy generated from a high surface air-sea temperature and moisture difference in the initial model system as well as in the spin-up process.

The wind shear effect on the partitioned fluxes shown in Fig. 10 is more complex. First, the low-level peak negative net mass flux (below 2.2 km) in the stratiform cloud region is enhanced in 4N by strong wind shear, while positive net stratiform fluxes aloft (maximum near 9.3 km) are slightly weakened. For the convective region, the wind shear effect does not appear to alter net mass fluxes (all positive) but shifts the level of maximum flux downward. For the cloud-free area, the strong wind shear however reduces the intensity of negative net fluxes in 4N, which is a combined effect of weakened upward and downward fluxes (not shown). The respective upward and downward mass fluxes for both stratiform and convective cloud areas are strengthened in 4N, especially in the stratiform area (not shown). In the final stages, Fig. 10b shows that net mass fluxes weaken more in 4N than 4M for the stratiform, convective cloud and cloud-free areas, especially for the positive net fluxes in the lower levels of convective cloud areas. Actually, in stratiform cloud areas, the respective upward and downward mass fluxes in 4N remain strong toward the final stage due to the strong wind shear, while the respective fluxes in 4M become much weaker toward the end. In convective cloud areas, the wind shear effect moderately enhances the upward and downward mass fluxes, but the fluxes are much weaker in this final stage compared to the initial stage.

4. Thermodynamic Budget Analysis

The horizontally integrated budget equations (1) and (2) listed in section 2.3 can be further vertically integrated for budget computations for heat and moisture over the entire model domain. The model-domain-integrated vertical eddy flux convergence/divergence terms for both potential temperature and water vapor, $-\left\langle \frac{1}{\bar{\rho}} \frac{\partial}{\partial z} \bar{\rho} w' \theta' \right\rangle$ and $-\left\langle \frac{1}{\bar{\rho}} \frac{\partial}{\partial z} \bar{\rho} w' q_v' \right\rangle$, respectively, (where angle brackets denote vertically averaged) vanish over the entire domain, except for contributing to the respective surface sensible and latent heat fluxes (denoted as SHF and LHF, respectively,

hereafter) from the ocean surface. Two major objectives are presented in this section through thermodynamic budget analysis. First, the physical processes that determine how the quasi-equilibrium states of temperature and water vapor are approached (beginning stage) and maintained (final stage) are examined in section 4.1. Second, the associated physical processes accounting for the impact on the quasi-equilibrium states by various horizontal wind structures are discussed in section 4.2.

4.1 *Thermodynamic budget before and during quasi-equilibrium states*

Tables 3 and 4 list the domain averaged moist static energy for the initial and final 10 days of integration of the six runs, respectively. In the beginning stage for the cold/dry run 1M, the strong net radiative cooling dominates over the heating from both net large-scale temperature forcing (more heating by C_t than cooling by $-LSF_t$) and sensible heat flux leading to net cooling in temperature tendency, while the moistening from latent heat flux exceeds the drying from net large-scale moisture forcing (more drying by $-C_q$ than moistening by LSF_q) to produce net moistening (Table 3). Overall, in terms of moist static energy, the positive contribution from both latent and sensible heat fluxes tends to compensate for the strong net radiative cooling, while the net heating due to net large-scale temperature forcing fully balances the net cooling (drying) by net large-scale moisture forcing. In the final 10 days (Table 4), all of the components are reduced in magnitude compared to the initial stage, especially latent heat flux and net large-scale temperature forcing, which results in the very low moist static energy for 1M. The strong reduction in latent heat flux due mainly to the greatly weakened wind speed, weakens the convection which reduces the net heating by microphysical processes, especially that by the freezing process (C_t is found reduced in magnitude 8 W m^{-2} more than $-C_q$). Compared to the cold/dry run 1M, the mild/moist run 4M has a significant enhancement in latent heat flux (8.93 W m^{-2}) and net large-scale temperature forcing (7.79 W m^{-2}) over other physical processes in the beginning stage (Table 3). These two major processes, however, weaken in the final stage of 4M (Table 4) as a quasi-equilibrium state is reached. A reduced air-sea humidity difference (due to increased air humidity) along with the weak surface wind accounts for the weakened latent heat flux. Net large-scale moisture forcing, however, increases relatively (less drying) in the final stage as the reduction in drying due to $-C_q$ outweighs the reduction in moistening due to LSF_q .

Similarly, latent heat flux and net large-scale temperature forcing are also the two major physical processes that account for the shift in regime from mild/moist to warm/wet for the mixed-wind shear runs 4M and 7M (Table 3). Latent heat flux dominates the increase in water vapor while net condensation (C_t) dominates the temperature increase ($-LSF_t$ is almost unchanged). In the final stage of 7M, latent heat flux weakens significantly, while net large-scale forcing in temperature/moisture decreases/increases considerably (compared to the beginning stage). Consistent with the finding in 4M, net large-scale forcing in moisture plays a more important role in the moisture budget as latent heat flux weakens near the end. The three warm/wet runs with strong wind shear, i.e., 1N, 4N and 7N, do not behave exactly the same as 7M does. These three runs all possess large heating by net large-scale temperature forcing in the beginning stage as 7M does. They have a higher contribution to the moisture budget by net large-scale moisture forcing (larger LSF_q), but smaller latent heat flux than 7M. Also note that the stronger net radiative cooling in 7M results in a relatively smaller temperature tendency than 1N, 4N and 7N. The stronger cooling by net radiation in 7M may be due to the higher percentage of precipitating convective clouds occurring in 7M than in 1N, 4N and 7N. On the other hand for the moisture budget, a smaller moisture tendency in 7M compared to 1N, 4N and 7N is mainly due to the greater intensification of net large-scale moisture forcing due to strong wind shear (in 1N, 4N and 7N) than that of latent heat flux due to strong surface winds (in 7M). In the final stage, net large-scale temperature forcing decreases (less heating by C_t than cooling by $-LSF_t$) as well as latent heat flux, while net large-scale moisture forcing increases (more moistening by LSF_q than drying by $-C_q$) for 1N, 4N and 7N (Table 4). Compared to the strong wind shear runs, 7M has more heating by sensible heat flux which compensates the larger cooling by net radiation. It also has stronger moistening by latent heat flux balanced by a relatively stronger drying by net large-scale forcing in moisture.

4.2 Impact on thermodynamic budget due to various horizontal wind structures

Results discussed in the previous section reveal that various horizontal wind structures play a crucial role in determining the quasi-equilibrium states by both the wind shear and surface wind speed effects. These effects can be further examined by comparing the heat and moisture budgets (for the initial and final 10-day periods as well as the 25-day integration) between deliberately paired runs either with different wind shear patterns (e.g., 4M with mixed-wind shear versus 4N with strong wind shear) or with different surface wind speeds (e.g., 1M with 1 ms^{-1} versus 4M with 4 ms^{-1}).

Several major findings are presented as follows without showing detailed numerical manipulations.

In terms of the impact of strong wind shear on the heat budget, net large-scale temperature forcing (involving a large amount of condensational heating offset mostly by a comparable vertical advective cooling) is found predominantly responsible for the temperature increase for runs with low surface wind speeds (i.e., from 1M to 1N, and 4M to 4N). Sensible heat flux plays a minor positive role in the warming, while net radiation offsets it with stronger longwave radiative cooling. An overall expanded cloud system (broadening and deepening) due to strong wind shear is found to enhance longwave emission above the cloud base and slightly reduce longwave cooling below it. On the other hand, shortwave radiation is enhanced above the cloud base (more absorption by the cloud) and diminished below it (more blockage by the cloud). The net radiative effect is negative since the shortwave heating is overpowered by the longwave cooling. Between 7M and 7N (with a strong surface wind), the net radiation becomes the dominant process, while the net large-scale forcing remains a positive but much less crucial term. This net radiative gain due to strong wind shear with a high surface wind is attributed to more shortwave heating than longwave cooling throughout the entire integration. Based on analyses for various periods (the initial, final 10-day and the entire 25-day), it is found that the net large-scale temperature forcing remains the dominant process accounting for the wind shear effect from the beginning to the end for runs with weaker surface winds, while the net radiation remains the dominant process in runs with strong surface wind.

The impact due to various surface wind speeds on the heat budget is found significant only between runs with mixed-wind shear (i.e., from 1M to 4M, and 4M to 7M). The net large-scale temperature forcing and sensible heat flux are found the major and minor processes responsible for the increase in temperature tendency, while a net radiative cooling performs a negative effect. Accordingly, intensification in the net large-scale forcing is mainly due to the enhanced net condensation (C_t) originating from enlarged convective clouds, while the net radiative cooling comes primarily from a longwave radiative cooling, which is also a response to the extensive convective clouds. These two major physical processes (constructively and destructively), however, have a stronger impact in the final stage than in the initial stage, which is consistent with a finding that the enhancement of convective clouds occurs more in the later stage than in the earlier stage.

In the moisture budget for the entire 25-day period, latent heat flux and net large-scale moisture forcing are found the two dominant processes responsible for the increased moisture tendency due to strong wind shear. Latent heat flux (positive) dominates net large-scale moisture forcing (negative) in the moisture increase for runs from 1M to 1N. Such a dominance by latent heat flux is mainly due to a great surge in surface wind speed by strong wind shear, even at the expense of a moderate loss in sea-air humidity difference. From 4M to 4N, latent heat flux weakens its (still positive) contribution due to a reduced surge in surface wind speed, while the contribution by net large-scale forcing in moisture is enhanced to be positive. From 7M to 7N, net large-scale forcing in moisture becomes the dominant process (positive) over the further weakened latent heat flux (negative). However note that during the very early stage (not shown), latent heat flux still slightly dominates over net large-scale moisture forcing from 7M to 7N when the sea-air humidity difference is still critically large, while the latter becomes the sole major process in the final stage when the sea-air humidity difference significantly drops. Overall, latent heat flux is the dominant process that accounts for the wind shear effect in runs with weaker surface winds, while net large-scale forcing dominates in runs with stronger surface winds. This is mainly because the surface wind speed surge due to strong wind shear flattens out as the prescribed minimum wind speed increases closer to those in the strong wind shear runs (about $7-8 \text{ ms}^{-1}$).

Similar to its impact on the heat budget, the minimum surface wind effect on the moisture budget is significant only between runs with mixed-wind shear. Latent heat flux is found the dominant process over net large-scale moisture forcing responsible for the variation of moisture tendency between the mixed-wind shear runs from the beginning period to the end. Apparently, embedded surface fluxes are necessary for a convective system to develop into a quasi-equilibrium state. Overall, the net large-scale forcing (in both temperature and moisture) and surface fluxes are crucially responsible for the dramatic discrepancy found in modeled quasi-equilibrium states, e.g., that between S94 and G96. However, the role sensible heat flux plays in the heat budget is much less significant than what latent heat flux does in the moisture budget and so too in the thermodynamic quasi-equilibrium system.

5. Summary

The schematic diagram shown in Fig. 11 indicates the major physical components and the associated physical processes involved in the radiative-convective system that was simulated and discussed in this study. The imposed vertical wind shear condition (mixed-wind shear or strong wind shear), minimum surface wind speed for computing surface fluxes, and radiation are the three major components that determine the quasi-equilibrium temperature and water vapor fields. The imposed wind shear patterns and minimum wind speeds are particularly responsible for generating such dramatically diverse quasi-equilibrium states as, for example, were found between S94 and G96. Conditions associated with strong wind shear or a large prescribed minimum wind speed tend to produce a warm/wet regime, while a mixed-wind shear and a small prescribed minimum wind speed create a mild/moist or cold/dry regime. Radiation is found necessary in establishing the aforementioned quasi-equilibrium states but is not crucial in the dramatic changes among them.

Specific features of convective systems associated with various quasi-equilibrium states are as follows. In terms of cloud area coverage, latent heat flux (minimum wind speed) plays a decisive role in extending erect convective clouds for mixed-wind shear runs (in three regimes). For strong wind shear runs (all in the warm/wet regime), both stratiform (well-organized type, particularly) and convective clouds expand their area coverage as minimum wind speed increases, though stratiform clouds dominate convective clouds in area coverage. The strong wind shear provides the cloud system with two distinct effects: first, an environment favorable for the enhancement of large-scale forcing that produces more well-organized clouds, and second, a strong surface wind that strengthens surface fluxes which generate more convective clouds. Nevertheless, a higher regime is found to produce a larger rainfall amount, as convective clouds are the leading source of rainfall over stratiform clouds. Based on rainfall histograms, strong wind shear runs are dominated by low rainrates ($0 - 2 \text{ mm hr}^{-1}$) in both amount and frequency, while mixed wind shear runs are dominated by slightly higher rainrates ($2 - 4 \text{ mm hr}^{-1}$) in amount. However, the high rainrates (e.g., no less than 24 mm hr^{-1}) together contribute a large amount of rainfall even though they occur infrequently. They are associated with the most intense convective clouds that have high precipitation efficiency.

The convective system with mixed-wind shear (mainly shallow and deep convective cells) is driven by a light-westerly net steering effect. The more complex system with strong wind shear moves as follows: the shallow convective clouds propagate westward due to low-level easterly flow, while the well-organized stratiform clouds move eastward in response to gravity waves that move eastward in a duct under the westerlies aloft. The large-scale zonal wind shear plays a crucial role in determining the formation as well as the migration of radiative-convective systems not only by its wind intensity and vertical gradient but also by the direction that it veers with height. A cold/dry run of low CAPE reaches a quasi-equilibrium state associated with a lower atmosphere that is more static-unstable (dry-adiabatic), while the warm/wet runs of high CAPE reach a state that is more moist-unstable (pseudo-adiabatic) in the lower atmosphere. Cloud-scale eddies act as a hydrodynamic “vehicle” that redistributes (cascades) the heat and moisture vertically by means of upward and downward convective motions. They assist in balancing the heat (Q_1) and moisture (Q_2) budgets and in reaching a quasi-equilibrium state. A stronger circulation (upward and downward fluxes) is generally found in the strong wind shear runs compared to the mixed-wind runs, which provides sufficient vertical momentum for a stronger large-scale forcing process.

Several features involving physical processes that account for the genesis and maintenance of quasi-equilibrium states as well as the effects from the associated horizontal wind structures are obtained based on thermodynamic budget analyses. For the cold/dry run 1M of mixed-wind shear, in the beginning stage the positive contribution from both latent and sensible heat fluxes tends to compensate for the strong net radiative cooling, while the net heating due to net large-scale temperature forcing fully balances the net cooling (drying) by net large-scale moisture forcing. In the final stage, all of the components are reduced in magnitude, especially latent heat flux and net large-scale temperature forcing, which leads to quasi-equilibrium states. As the minimum surface wind is increased, a significant enhancement in latent heat flux and net large-scale temperature forcing over other physical processes occurs in the beginning stage that eventually results in the shift in regime from cold/dry to mild/moist to warm/wet. The three warm/wet runs with strong wind shear, i.e., 1N, 4N and 7N, behave differently from 7M. In the beginning stage, the three runs with strong wind shear all possess large heating by net large-scale temperature forcing as does 7M, but they have smaller net radiative cooling. They also have a higher contribution to the moisture budget from net large-scale moisture forcing, but smaller latent heat flux than

7M. In the final stage of the strong wind shear runs, net large-scale temperature forcing decreases as well as latent heat flux, while net large-scale moisture forcing increases.

In determining the quasi-equilibrium state, the wind shear effect has a prominent impact on runs with lower minimum wind speeds, while the minimum surface wind effect is crucial for mixed-wind shear runs. Net large-scale forcing in both temperature and moisture, and latent heat flux are the major physical processes that account for these two effects. Latent heat flux dominates for both a strong wind shear and a strong minimum wind speed effect on the moisture budget, while net large-scale forcing in moisture dominates when the wind shear effect is relatively weaker (between runs 7N and 7M with a high minimum wind speed). Net large-scale forcing in temperature on the other hand is the primary process that determines the temperature equilibrium state associated with a strong wind shear or a strong minimum wind speed effect.

These simulations are based on a more idealized than realistic environment, several important features (claimed in the four major goals of this paper) have, however, been identified and presented. In this study, the modeled quasi-equilibrium state is found to be sensitive to two crucial components: sea surface fluxes (sensitive to the prescribed minimum wind speed) and the cloud system organization (dependent on the vertical wind shear). Therefore, improving the performance of our model simulations by better understanding the physical, dynamic and microphysical processes involved in radiative-convective systems as well as carefully employing physically realistic data (e.g., reliable in-situ observations) for the boundary and initial conditions is our major goal for the future.

6. Acknowledgments

The authors wish to thank Mr. S. Lang for reading the manuscript and Dr. S. Shige for useful discussions. This study is supported by the NASA Headquarters Physical Climate Program and by the NASA TRMM project. The authors are also grateful to Dr. R. Kakar (NASA/HQ) for his support of this research. Special thanks also go to three anonymous reviewers for their constructive comments that improved the clarity of presentation in this paper.

Acknowledgment is also made to NASA/Goddard Space Flight Center for computer time used in the research.

7. References

- Cheng, C.-P., and R. A. Houze Jr., 1979: The distribution of convective and mesoscale precipitation in GATE radar echo patterns. *Mon. Wea. Rev.*, **107**, 1370-1381.
- Chou, M. D., and A. Arking, 1980: Computation of infrared cooling rates in the water vapor bands. *J. Atmos. Sci.*, **37**, 855-867.
- _____, and _____, 1984: Broadband water vapor transmission functions for atmospheric IR flux computation. *J. Atmos. Sci.*, **41**, 1775-1778.
- Ferrier, B. S., J. Simpson, and W.-K. Tao, 1996: Factors responsible for precipitation efficiencies in midlatitude and tropical squall simulations. *Mon. Wea. Rev.*, **124**, 2100-2125.
- Gamache, J. F., and R. A. Houze Jr., 1983: Water budget of a mesoscale convective system in the Tropics. *J. Atmos. Sci.*, **40**, 1835-1850.
- Grabowski, W. W., M. W. Moncrieff, and J. T. Kiehl, 1996: Long-term behavior of precipitating tropical cloud systems: A numerical study. *Quart. J. Roy. Meteor. Soc.*, **122**, 1019-1042.
- Held, I. M., R. S. Hemler, and V. Ramaswamy, 1993: Radiative-convective equilibrium with explicit two-dimensional moist convection. *J. Atmos. Sci.*, **50**, 3909-3927.
- Houze, R. A., Jr., 1977: Structure and dynamics of a tropical squall-line system. *Mon. Wea. Rev.*, **105**, 1540-1567.
- Islam, S., R. L. Bras, and K. A. Emanuel, 1993: Predictability of mesoscale rainfall in the Tropics. *J. Appl. Meteor.*, **32**, 297-310.
- Li, X., C.-H. Sui, K.-M. Lau, and M.-D. Chou, 1999: Large-scale forcing and cloud-radiation interaction in the tropical deep convective regime. *J. Atmos. Sci.*, **56**, 3028-3042.

Lin, Y.-L., R. D. Farley, and H. D. Orville, 1983: Bulk parameterization of the snow field in a cloud model. *J. Climate Appl. Meteor.*, **22**, 1065-1092.

Nakajima, K., and T. Matsuno, 1988: Numerical experiments concerning the origin of cloud clusters in the tropical atmosphere. *J. Meteor. Soc. Japan*, **66**, 309-329.

Peng, L., C.-H. Sui, K.-M. Lau, and W.-K. Tao, 2001: Genesis and evolution of hierarchical cloud clusters in a two-dimensional cumulus resolving model. *J. Atmos. Sci.*, **58**, 877-895.

Randall, D. A., Q. Hu, K.-M. Xu, and S. K. Krueger, 1994: Radiative-convective disequilibrium. *Atmos. Res.*, **31**, 315-327.

Robe, F. R., and K. A. Emanuel, 1996: Dependence of tropical convection on radiative forcing. *J. Atmos. Sci.*, **53**, 3265-3275.

Rutledge, S. A., and P. V. Hobbs, 1984: The mesoscale and microscale structure and organization of clouds and precipitation in mid-latitude cyclones. XII: A diagnostic modeling study of precipitation development in narrow cold-frontal rainbands. *J. Atmos. Sci.*, **41**, 2949-2972.

Soong, S.-T., and Y. Ogura, 1980: Response of tradewind cumuli to large-scale processes. *J. Atmos. Sci.*, **37**, 2035-2050.

_____, and W.-K. Tao, 1980: Response of deep tropical clouds to mesoscale processes. *J. Atmos. Sci.*, **37**, 2016-2034.

Shige, S. and T. Satomura, 2001: Westward generation of eastward-moving tropical convective bands in TOGA COARE. *J. Atmos. Sci.*, submitted.

Sui, C.-H., K. M. Lau, W.-K. Tao, and J. Simpson, 1994: The tropical water and energy cycles in a cumulus ensemble model. Part I: Equilibrium climate. *J. Atmos. Sci.*, **51**, 711-728.

Tao, W.-K., and S.-T. Soong, 1986: A study of the response of deep tropical clouds to mesoscale processes: Three-dimensional numerical experiments. *J. Atmos. Sci.*, **43**, 2653-2676.

_____, and J. Simpson, 1993: The Goddard Cumulus Ensemble Model. Part I: Model description. *Terr. Atmos. Oceanic Sci.*, **4**, 35-72.

_____, _____, C.-H. Sui, S. Lang, J. Scala, B. Ferrier, M.-D. Chou, and K. Pickering, 1993: Heating, moisture and water budgets of tropical and mid-latitude squall lines: Comparisons and sensitivity to long wave radiation. *J. Atmos. Sci.*, **50**, 673-690.

_____, _____, _____, C.-L. Shie, B. Zhou, K. M. Lau, and M. Moncrieff, 1999: On equilibrium (climate) states simulated by cloud-resolving models. *J. Atmos. Sci.*, **56**, 3128-3139.

_____, C.-L. Shie, and J. Simpson, 2001: Comments on "A sensitivity study of radiative-convective equilibrium in the tropics with a convection-resolving model". *J. Atmos. Sci.*, **58**, 1328-1333.

Williams, E., and N. Renno, 1993: An analysis of the conditional instability of the tropical atmosphere. *Mon. Wea. Rev.*, **121**, 21-36.

Xu, K.-M., and D. A. Randall, 1996: Explicit simulation of cumulus ensembles with the GATE Phase III data: Comparison with observations. *J. Atmos. Sci.*, **53**, 3709-3736.

_____, and _____, 1999: A sensitivity study of radiative-convective equilibrium in the tropics with a convection-resolving model. *J. Atmos. Sci.*, **56**, 3385-3399.

Yamasaki, M., 1975: A numerical experiment of the interaction between cumulus convection and large-scale motion. *Pap. Meteor. Geophys.*, **26**, 63-91.

Yanai, M., S. Esbensen, and J. H. Chu, 1973: Determination of bulk properties of tropical cloud clusters from large-scale heat and moisture budgets. *J. Atmos. Sci.*, **30**, 611-627.

Ye, B., A. D. Del Genio, and K. K.-W. Lo, 1998: CAPE Variations in the current climate and in a climate change. *J. Climate.*, **56**, 3385-3399.

Table 1: Minimum surface wind speed and wind shear characteristics for six (three pairs) numerical experiments performed in this study. The two-letter naming convention identifies the two main parameters. For example, “1M” denotes a 1 ms^{-1} minimum wind speed (“1”) and mixed-wind shear (“M”), respectively. Experiments presented here all used the S94 sounding.

Run Name	Minimum Wind Speed	Vertical Wind Shear
1M	1 ms^{-1}	Mixed-wind
1N	1 ms^{-1}	Nudging
4M	4 ms^{-1}	Mixed-wind
4N	4 ms^{-1}	Nudging
7M	7 ms^{-1}	Mixed-wind
7N	7 ms^{-1}	Nudging

Table 2: Time-averaged (over 25 days of integration) domain rainfall amount and frequency (in percentage, %) distributions of the six runs for two rainrate ranges. The respective time-averaged rainfall amounts listed in each range are shown with both their values (units in mm hr^{-1}) and percentages (in %, normalized by the total time-averaged amounts from each run).

Run Name	Rainrate less than $4 \text{ mm hr}^{-1} \text{ grid}^{-1}$		Rainrate at least $24 \text{ mm hr}^{-1} \text{ grid}^{-1}$	
	Amount (mm hr^{-1} / %)	Freq. (%)	Amount (mm hr^{-1} / %)	Freq. (%)
1M	46.6 / 13.6	80.8	134.0 / 39.1	3.3
1N	75.5 / 18.0	85.0	144.6 / 35.4	2.3
4M	46.7 / 12.3	79.0	156.5 / 41.3	3.9
4N	74.9 / 18.4	85.3	140.8 / 34.7	2.2
7M	48.9 / 11.9	78.6	172.8 / 42.1	4.0
7N	80.6 / 19.6	85.8	132.9 / 32.3	2.0

Table 3: Moist static energy ($C_p dT + L_v dq_v$) budget for the initial 10 days of integration of the six runs. $C_p dT$ and $L_v dq_v$ are the local time change of temperature and water vapor, respectively. SHF, LHF, and SW-LW are sensible, latent heat flux, and net radiation, while $C_t - L_{SFt}$ and $L_{SFq} - C_q$ are the net large-scale forcing in temperature and water vapor, respectively. Units are in $W m^{-2}$.

Run Name	$C_p dT + L_v dq_v$	$C_p dT$	SHF	$C_t - L_{SFt}$	SW-LW	$L_v dq_v$	LHF	$L_{SFq} - C_q$
1M	-0.98	-4.50	7.52	35.36	-47.38	3.52	38.77	-35.25
1N	31.15	13.47	10.18	50.72	-47.43	17.68	52.50	-34.82
4M	10.55	2.21	8.99	43.15	-49.93	8.34	47.70	-39.36
4N	30.37	11.82	10.28	49.75	-48.21	18.55	53.25	-34.70
7M	21.51	9.04	10.22	50.48	-51.66	12.47	57.89	-45.42
7N	35.64	14.46	10.51	50.50	-46.55	21.18	53.83	-32.65

Table 4: Same as that in Table 3 except for the final 10 days of integration of the six runs. Units are in $W m^{-2}$.

Run Name	$C_p dT + L_v dq_v$	$C_p dT$	SHF	$C_t - L_{SFt}$	SW-LW	$L_v dq_v$	LHF	$L_{SFq} - C_q$
1M	-16.75	-11.22	5.12	20.93	-37.27	-5.53	19.87	-25.40
1N	7.89	2.62	7.32	45.12	-49.82	5.27	30.84	-25.57
4M	-1.23	-0.91	7.89	37.77	-46.57	-0.32	34.33	-34.65
4N	6.11	1.43	7.22	44.40	-50.19	4.68	30.07	-25.39
7M	5.34	2.53	9.01	46.22	-52.70	2.81	43.19	-40.38
7N	8.18	4.77	7.13	47.65	-50.01	3.41	30.16	-26.75

Figure captions:

Fig. 1. Scatter diagram of domain-averaged water vapor versus temperature at the quasi-equilibrium states (after twenty-five days of integration) for the eight runs listed in Table 1, along with results of S94 (“S”) and G96 (“G”). Three distinct thermodynamic regimes are shown by the three boxes and are characterized as follows: (1) warm/wet regime with T and q_v above 261.8°K and 67.0 mm, respectively, (2) mild/moist regime with T between 259.5°K and 260.0°K , and q_v between 57.5 mm and 60.0 mm, (3) cold/dry regime with T and q_v below 256.5°K and 48.1 mm, respectively.

Fig. 2. Two sets of 5-day averaged (dashed lines are for the initial 5 days and solid lines the final 5 days) wind shear profiles for 4M and 4N.

Fig. 3. Time-domain cross-sections of surface rainrate (mm/hr) over the final five days for (a) 4M, and (b) 4N.

Fig. 4. Instantaneous vertical cross-sections of the total cloud field for part of the domain (360 km out of a full domain of 768 km) for (a) 4M, and (b) 4N near the end of the simulations (23-days and 6-hours). Background wind vectors represent the total wind fields (zonal-mean wind plus perturbation wind for both the zonal and vertical directions) scaled by the designated “arrows” shown in the lower left corner.

Fig. 5. (a) Scatter diagram of 25-day total surface rainfall (mm/grid) versus rainfall contribution by stratiform clouds (in percentage) for the three pairs of experiments, (b) scatter diagram of 25-day convective versus stratiform cloud area coverage (in percentage) for the three pairs of experiments. Cloud area coverage is defined as the fraction of the cloud region (with or without precipitation) over the entire model domain.

Fig. 6. Rainfall amount histograms for (a) 4M, (b) 4N, and rainfall frequency (occurrence) histograms for (c) 4M, (d) 4N. The histograms presented are the averages of the instantaneous rainrate histograms (collected every 18 minutes) over the entire integration period (25 days).

Fig. 7. (a) Scatter diagram of a 5-day averaged (the final 5 days) surface relative humidity versus lower-tropospheric lapse rate of temperature for the three pairs of experiments, (b) same as (a) except for lower-tropospheric lapse rate of equivalent potential temperature. “cM” and “cW” are results from XR99 and are included in (a) for reference.

Fig. 8. Scatter diagram of CAPE versus wet-bulb potential temperature θ_w at the end of the simulation time for the three pairs of runs. “Y1”, “Y2”, and “Y3” are approximate results of Ye et al. (1998) and are included for comparison.

Fig. 9. Vertical profiles of individual time-mean (for the final 5 days) components in the heat budget for (a) 4M, and (b) 4N. Net heat condensation, large-scale temperature forcing, net radiation, and eddy heat flux convergence are denoted as “Ct”, “LSFt”, “SwLw”, and “EFCt”, respectively, in solid lines, while the sum of the first three components is denoted as “Res” by the dashed line; (c) and (d) are same as (a) and (b) except for the moisture budget. Net moisture condensation, large-scale moisture forcing, and eddy moisture flux convergence are denoted as “Cq”, “LSFq”, and “EFCq”, respectively, in solid lines, while the sum of the first two components is denoted as “Res” by the dashed line; (e) and (f) are same as (a) and (b) except for the Q1 and Q2 budgets. Q1 is denoted in a solid line and Q2 in a dashed line.

Fig. 10. Vertical profiles of horizontally-averaged mass fluxes for the pair of runs 4M and 4N for (a) the initial 5 days, and (b) the final 5 days, where dashed lines with symbols specify various cloud areas (“Con”, “Str”, and “Clr” denote convective, stratiform and cloud-free areas, respectively) for 4N, while the adjacent solid lines with symbols are for 4M. The total (upward and downward) horizontally-averaged mass fluxes (denoted by “Tot” in a solid line) are identical for 4M and 4N since a time-invariant horizontally-averaged vertical velocity field (all positive vertically) is prescribed in the model.

Fig. 11. A schematic diagram of the major physical components and associated physical processes involved in the radiative-convective system.

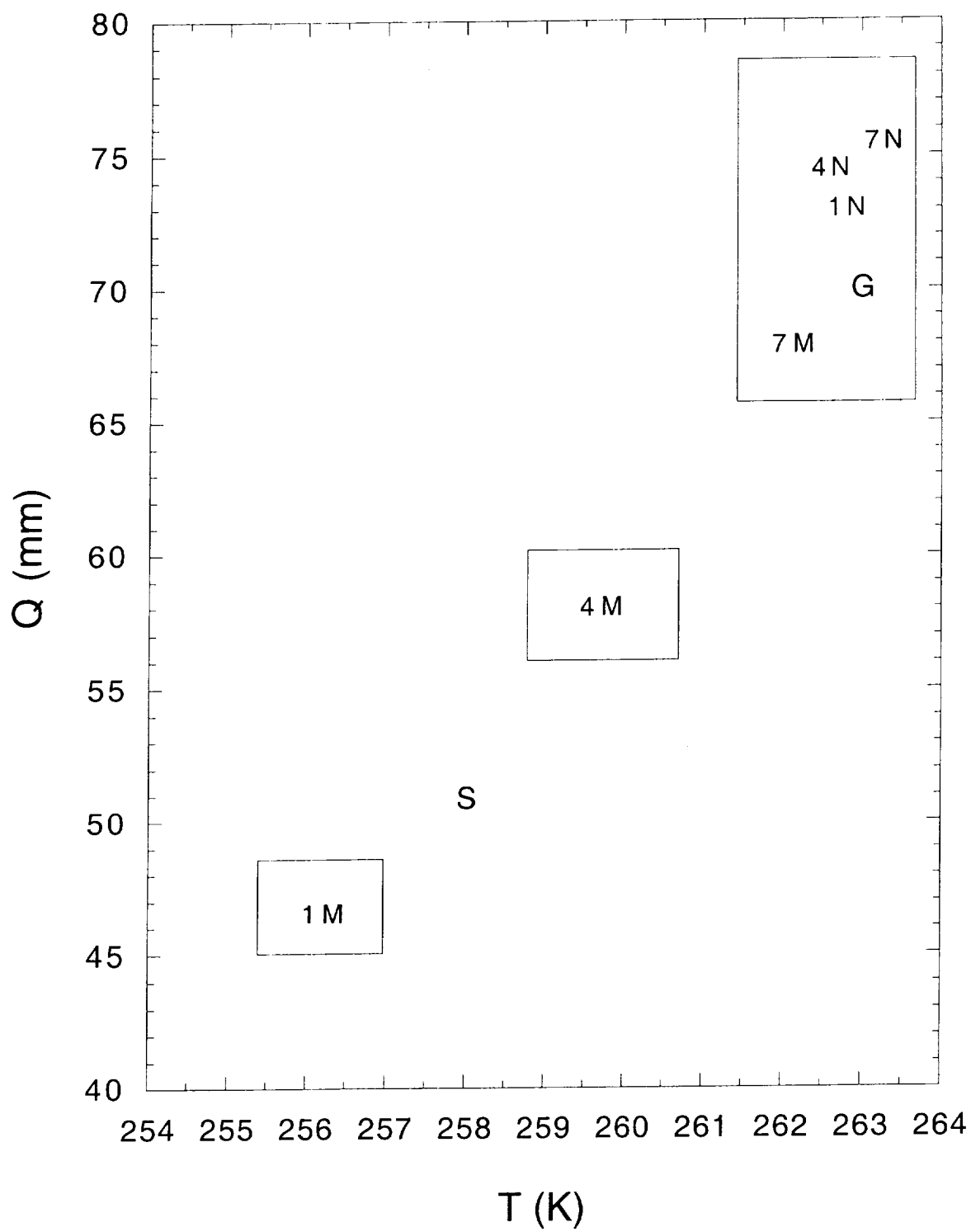


Fig. 1

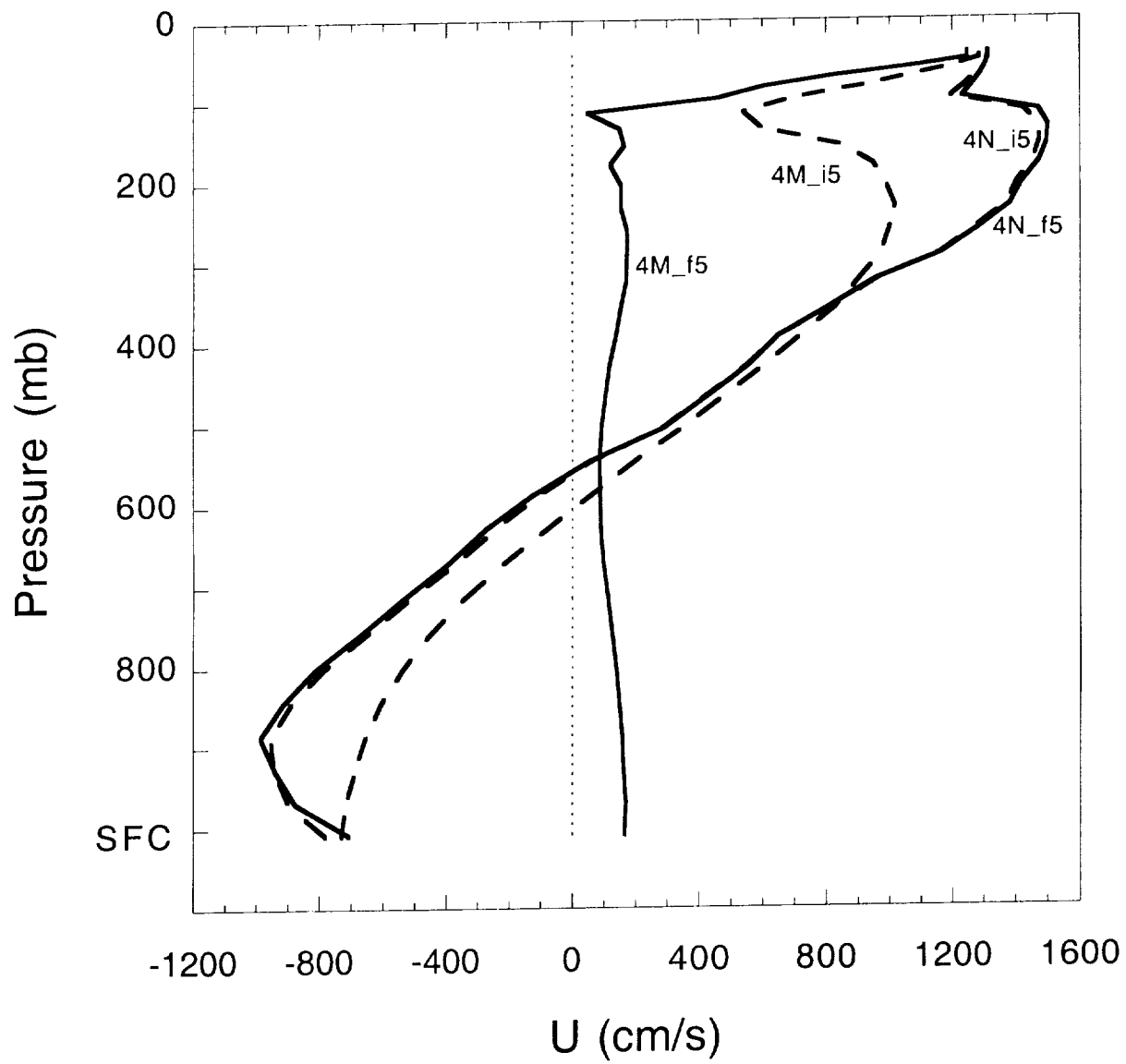


Fig. 2

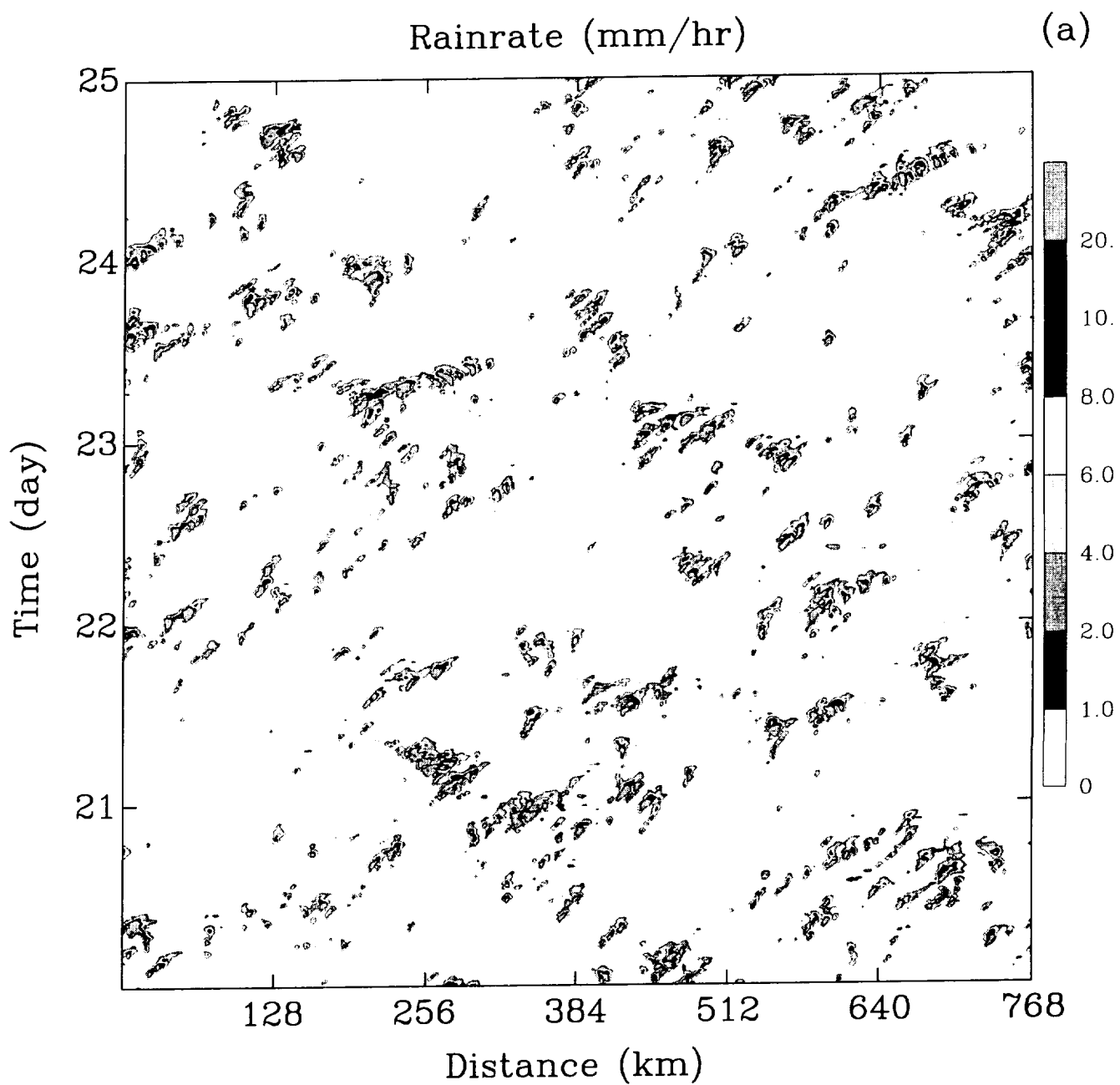


Fig. 3a

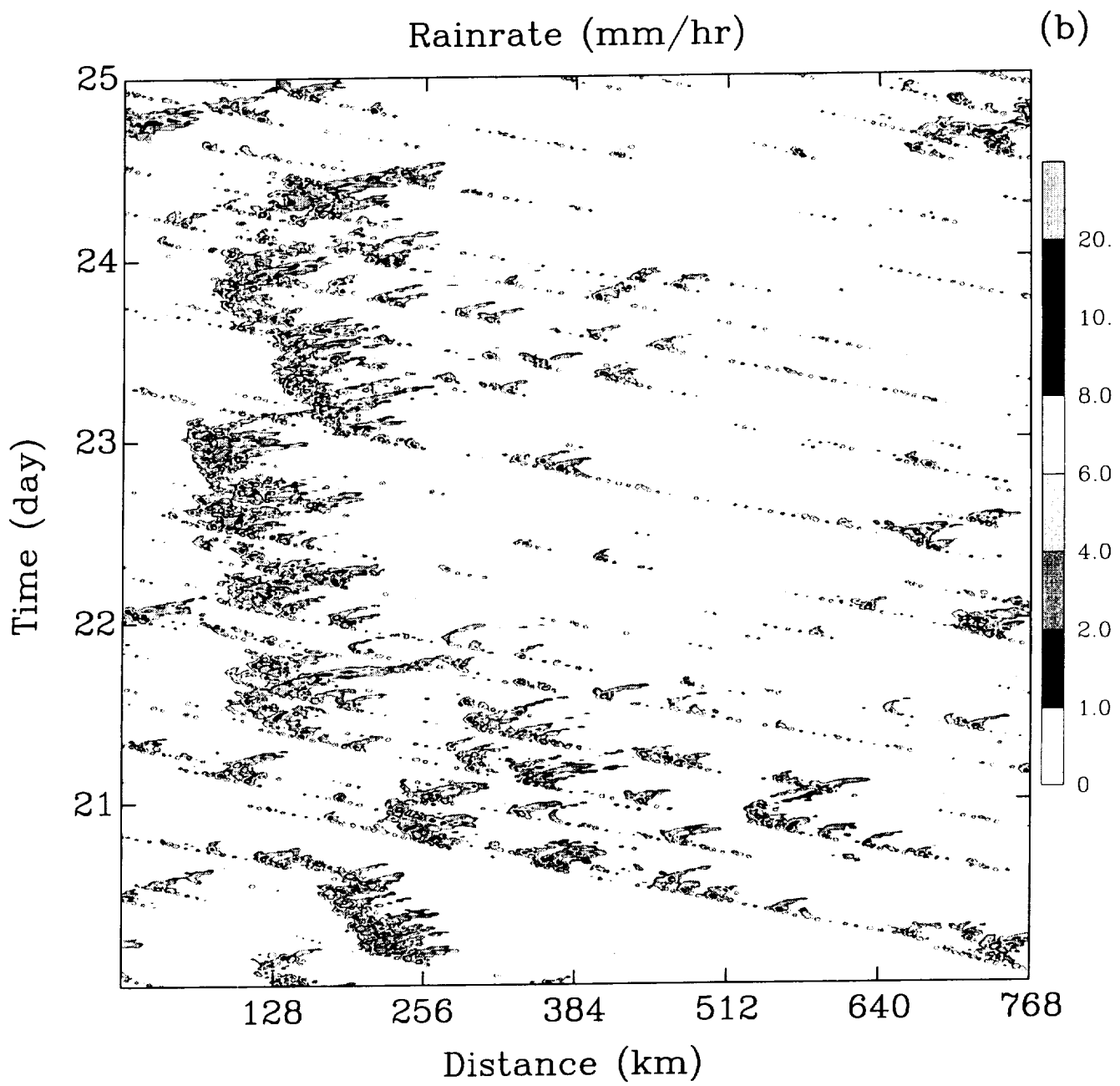


Fig. 3 b

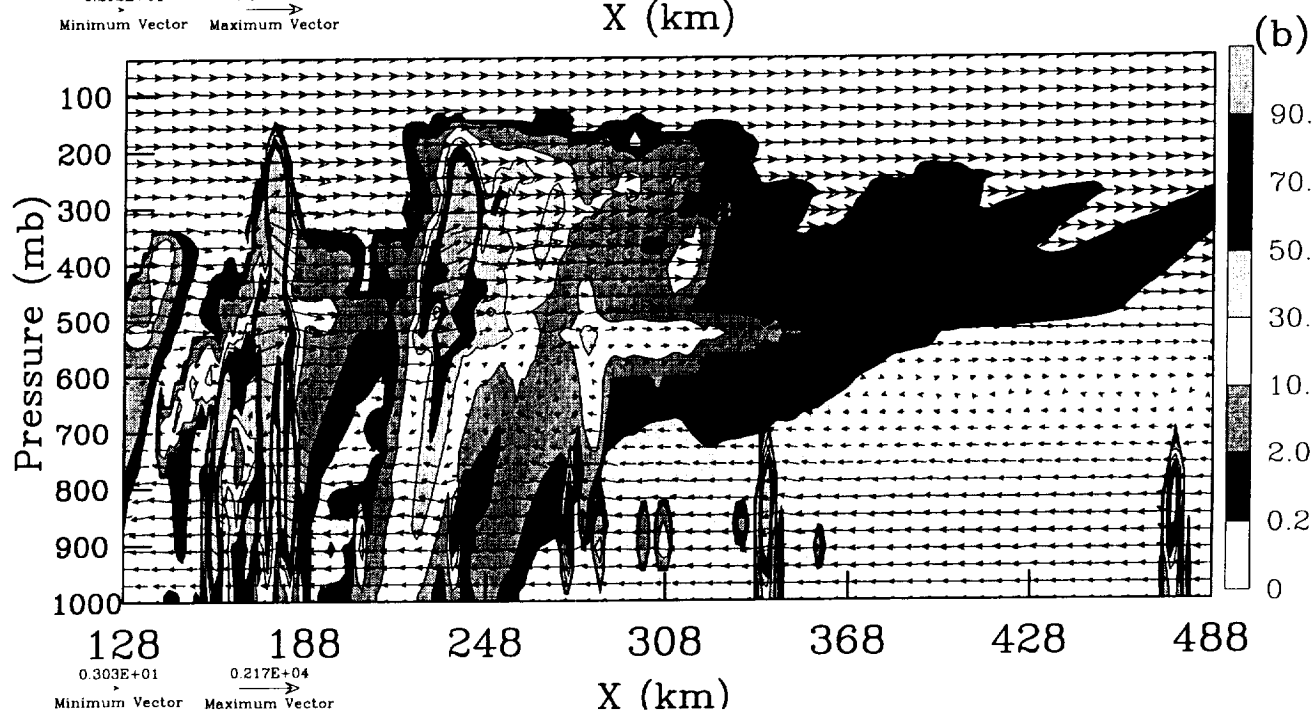
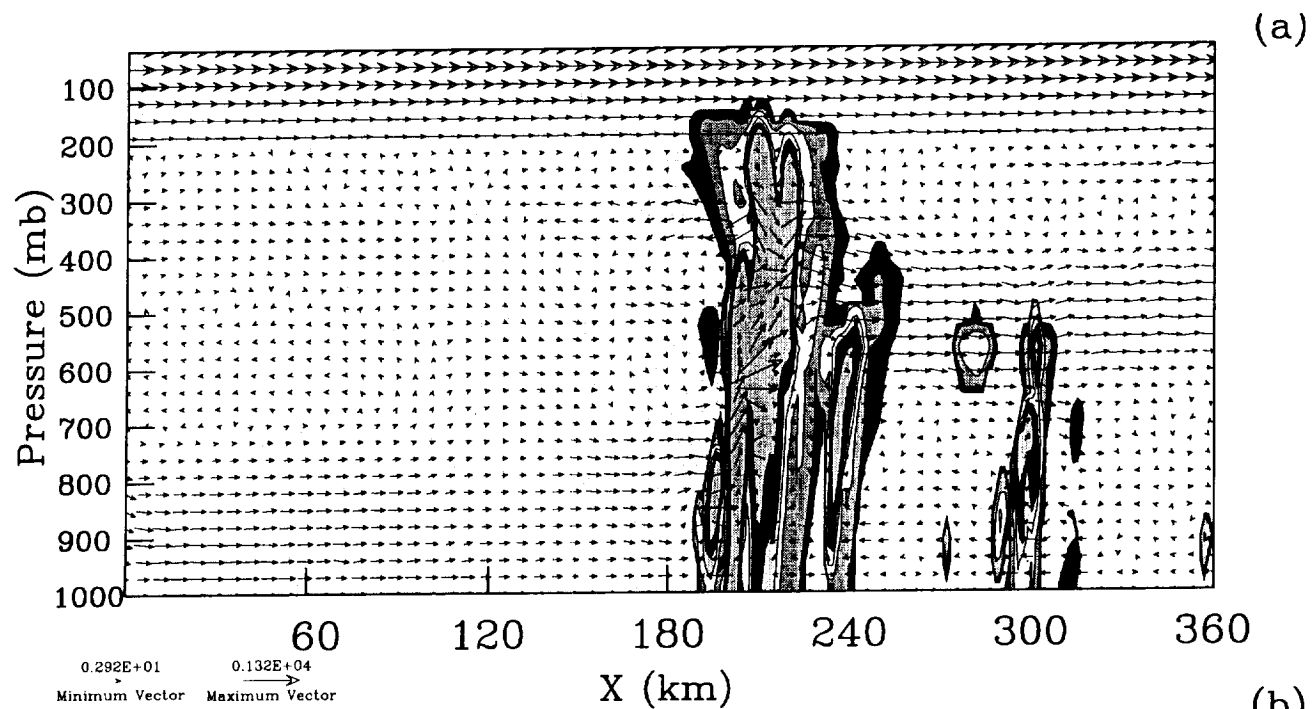


Fig. 4a, b

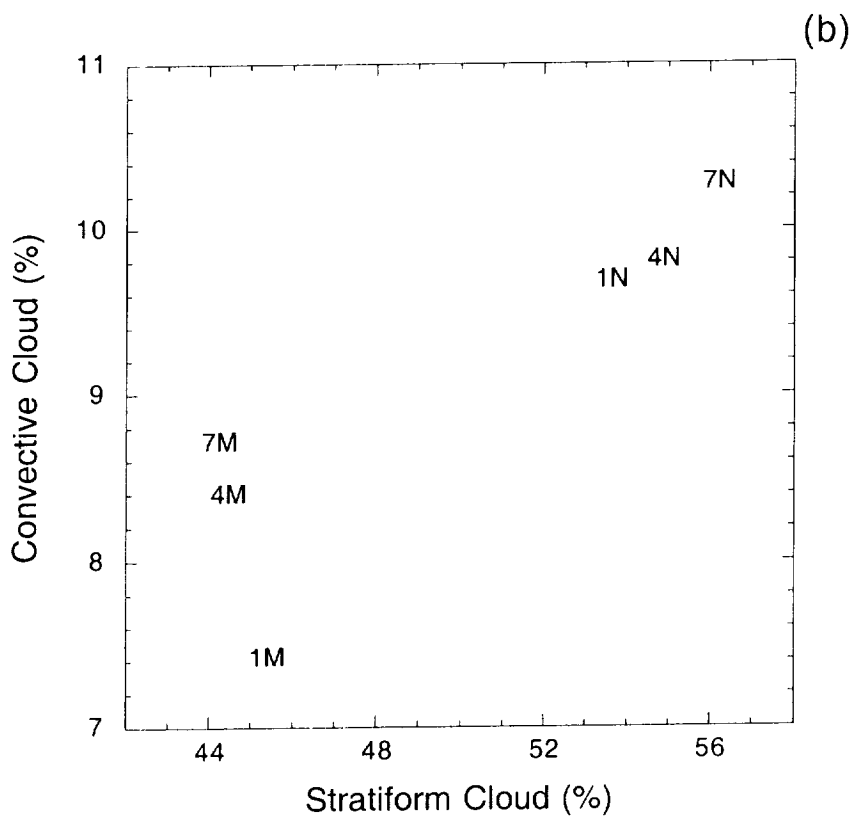
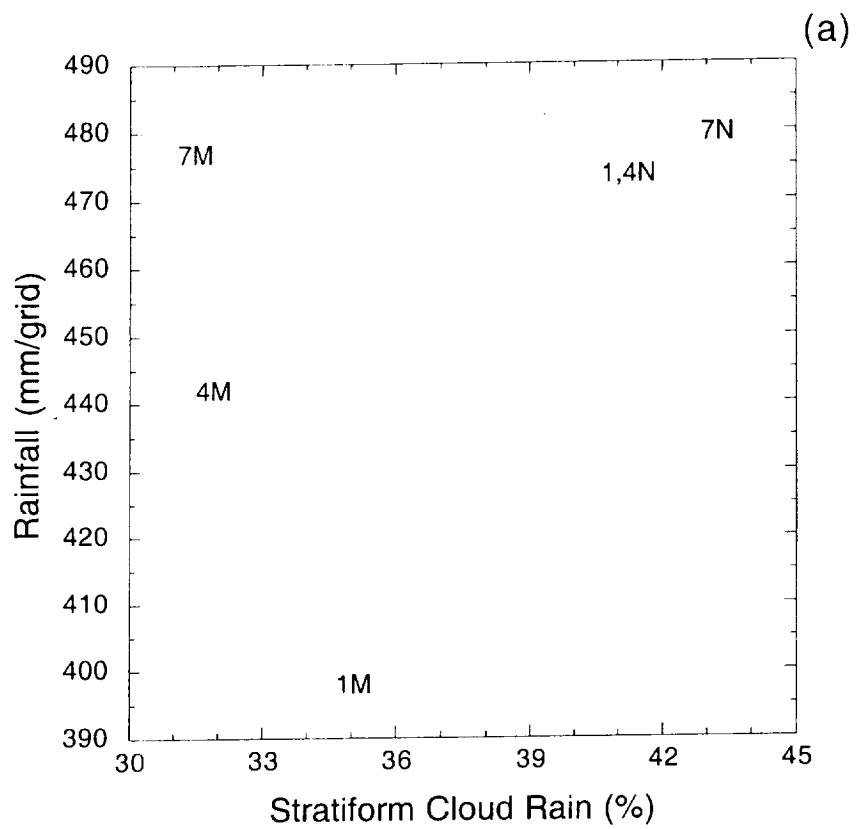


Fig. 5a,b

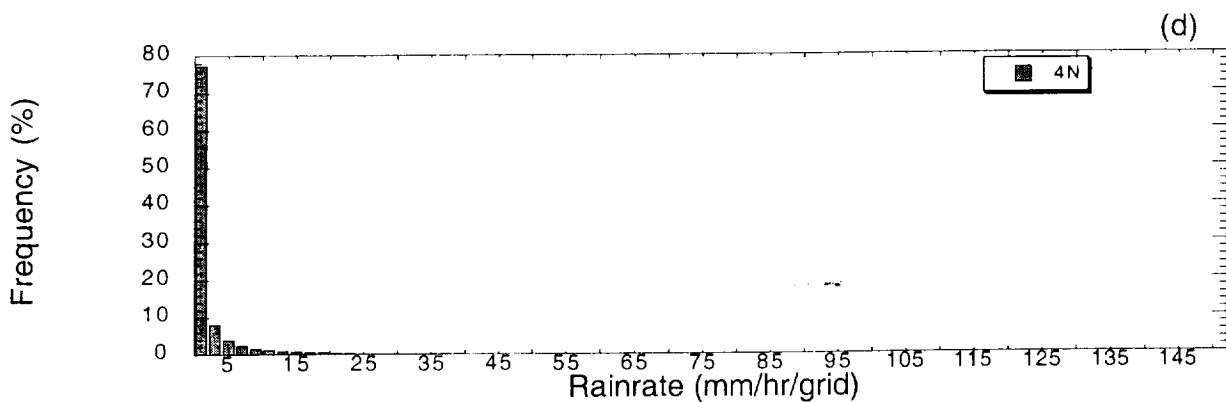
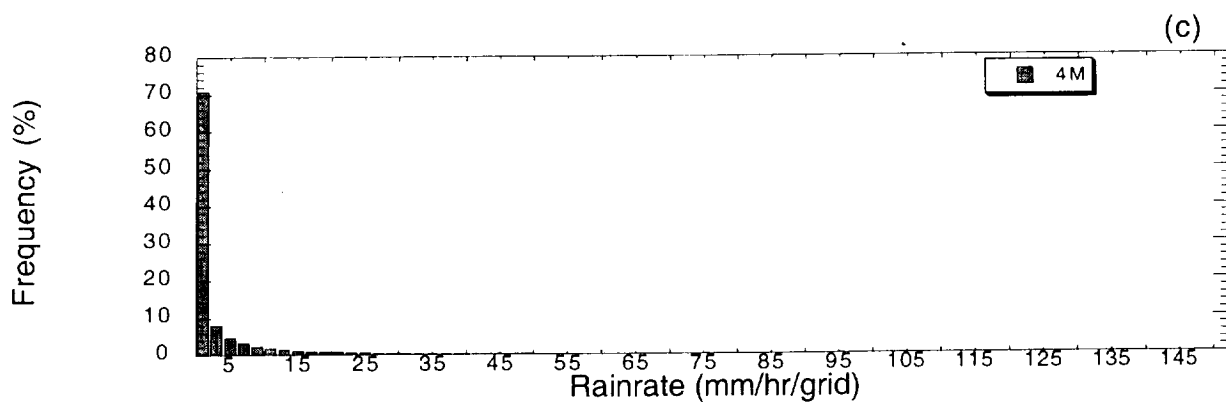
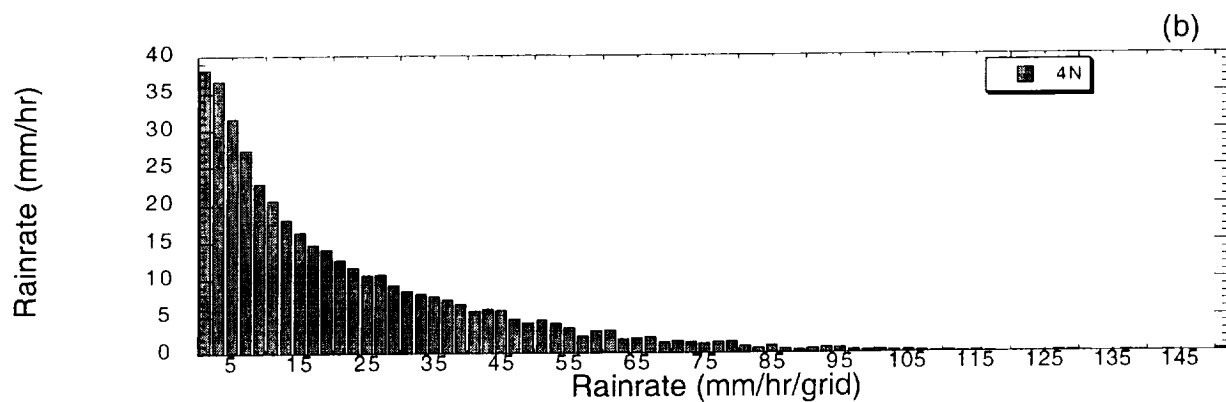
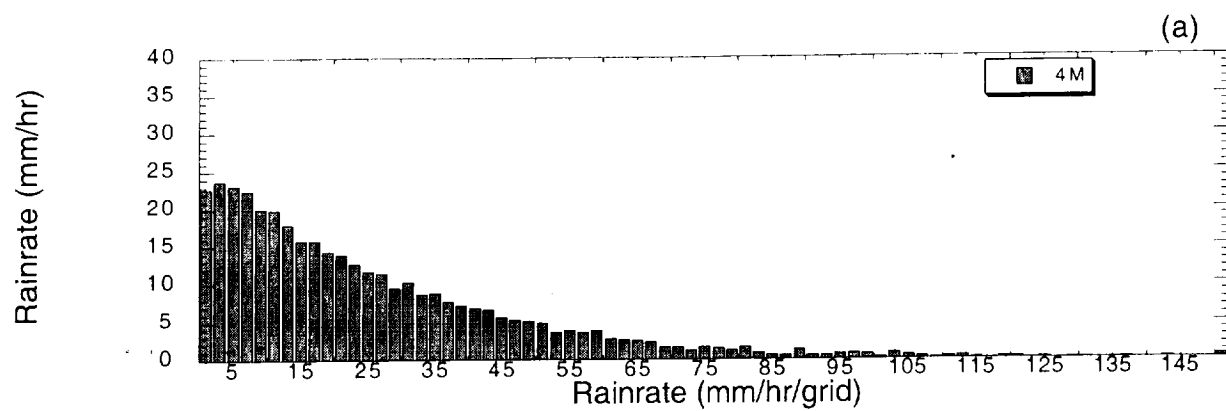


Fig. 6 a, b, c, d

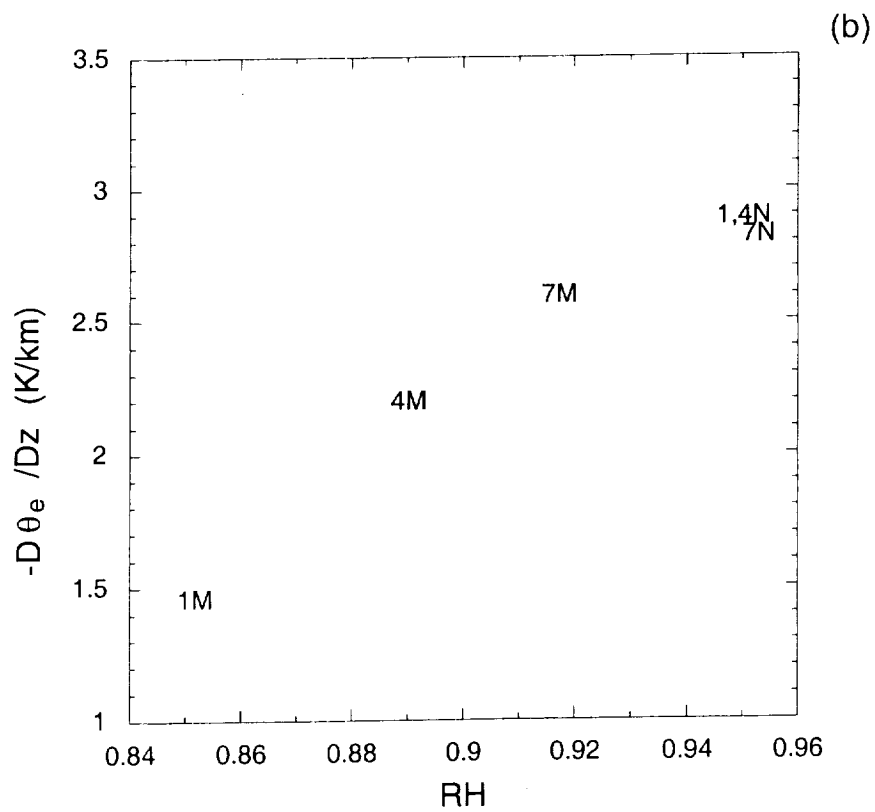
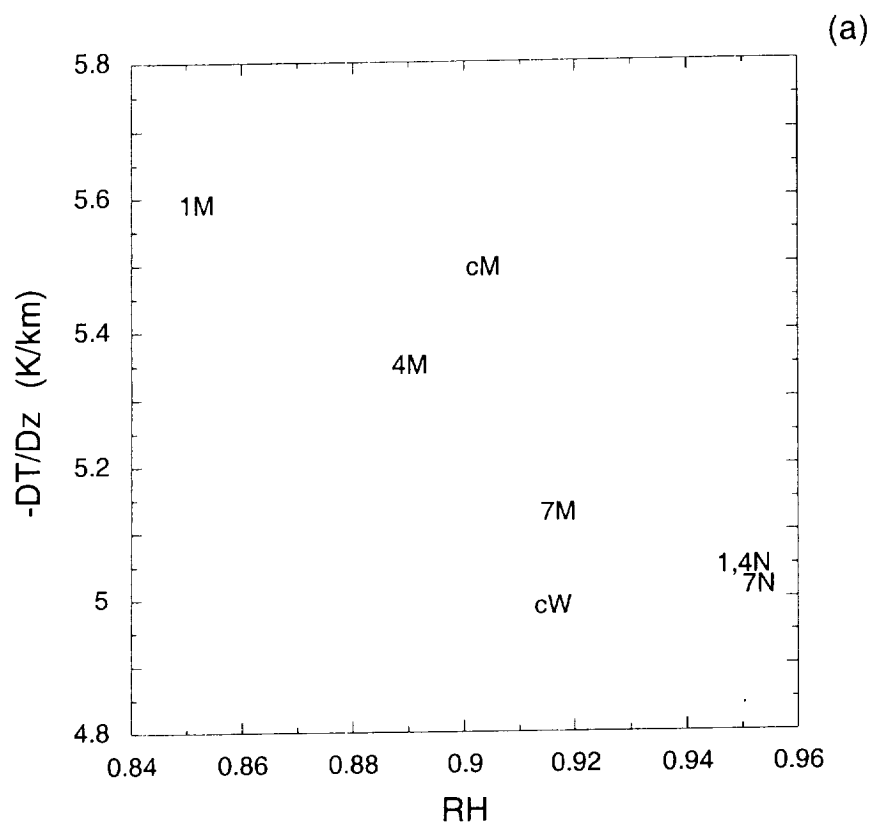


Fig. 7a,b

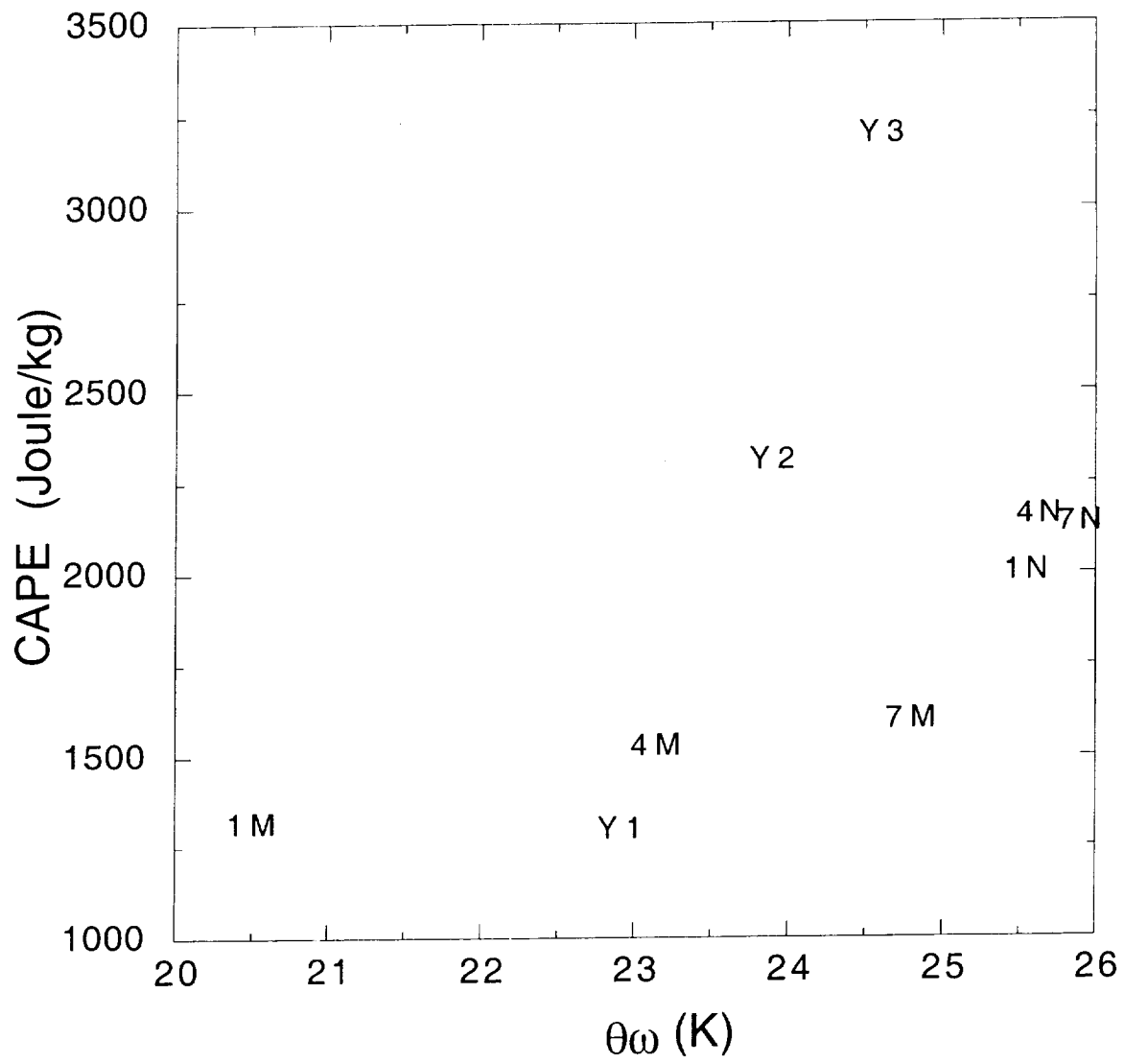


Fig. 8

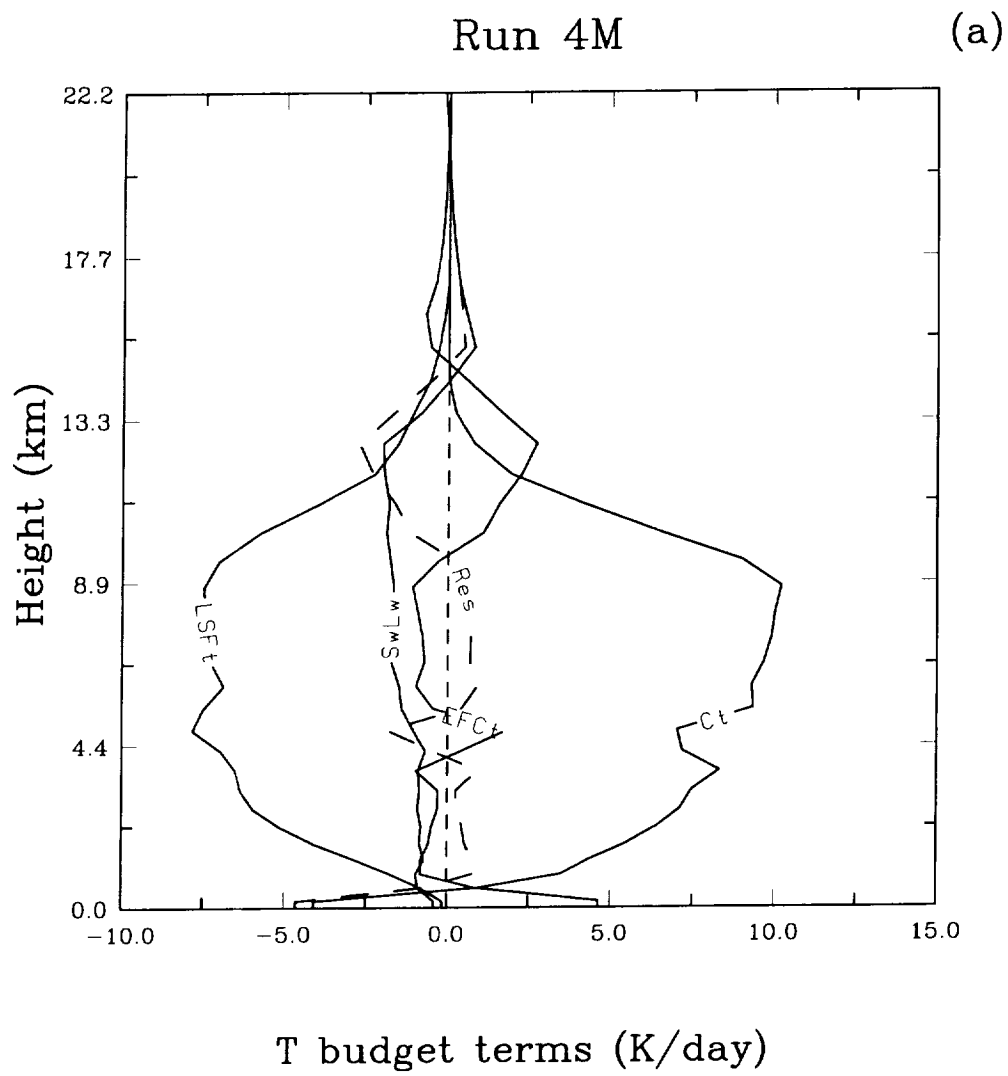


Fig. 9a

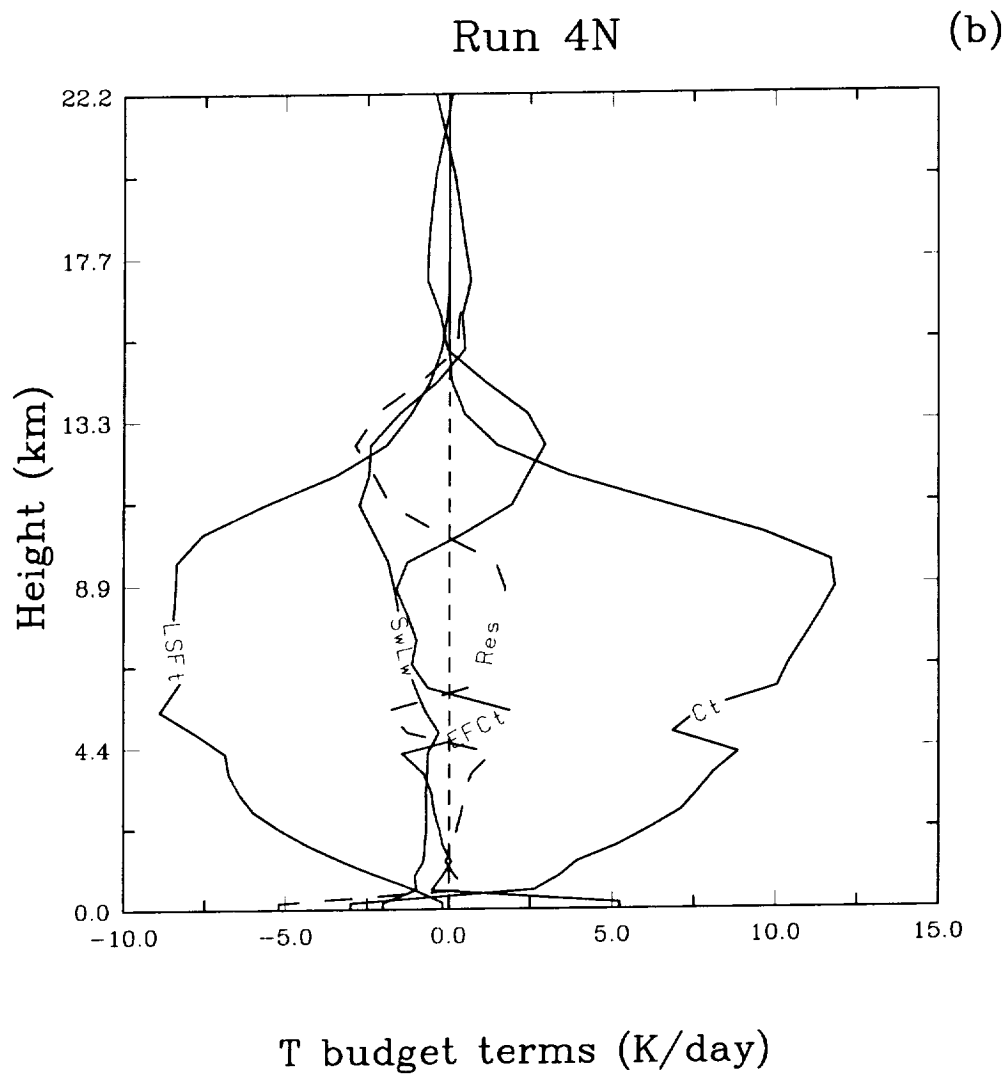


Fig. 9b

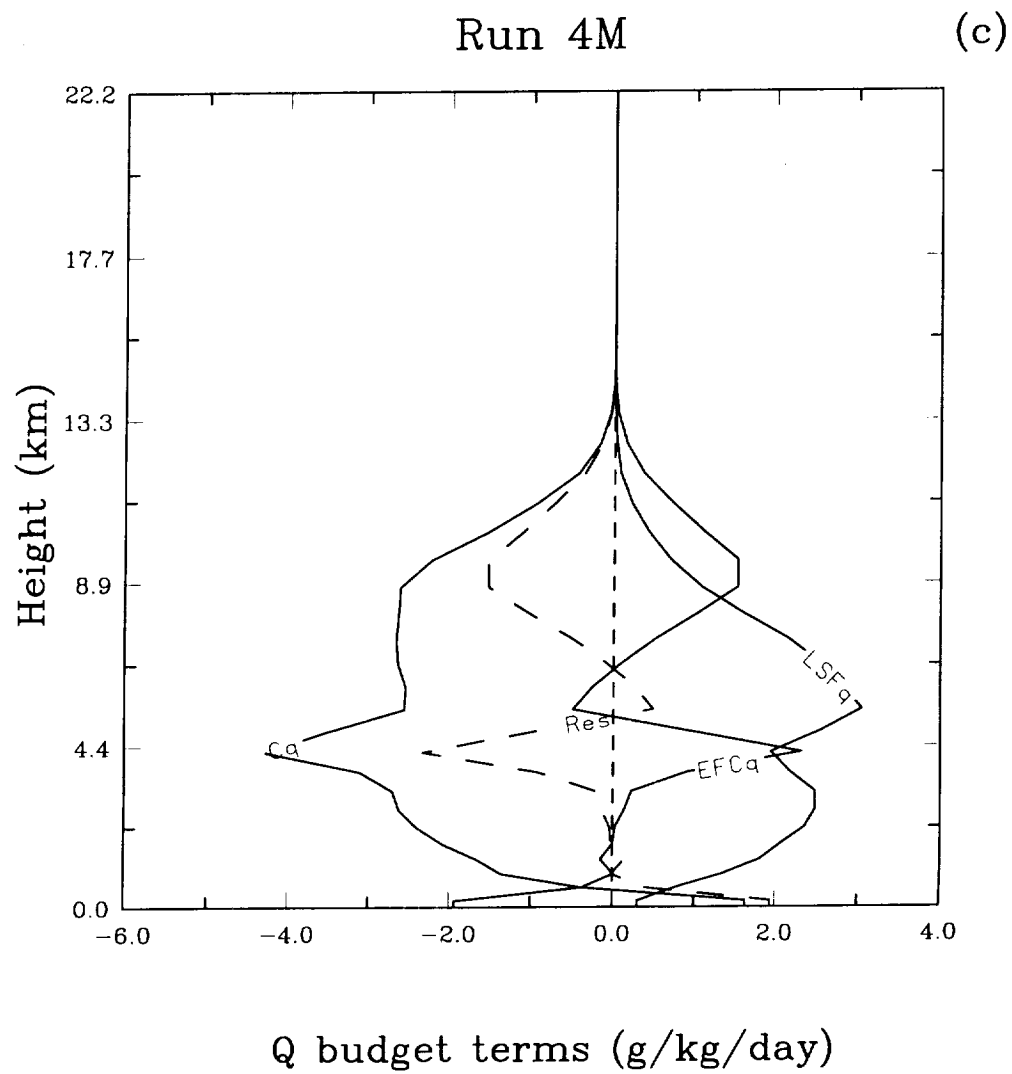


Fig. 9c

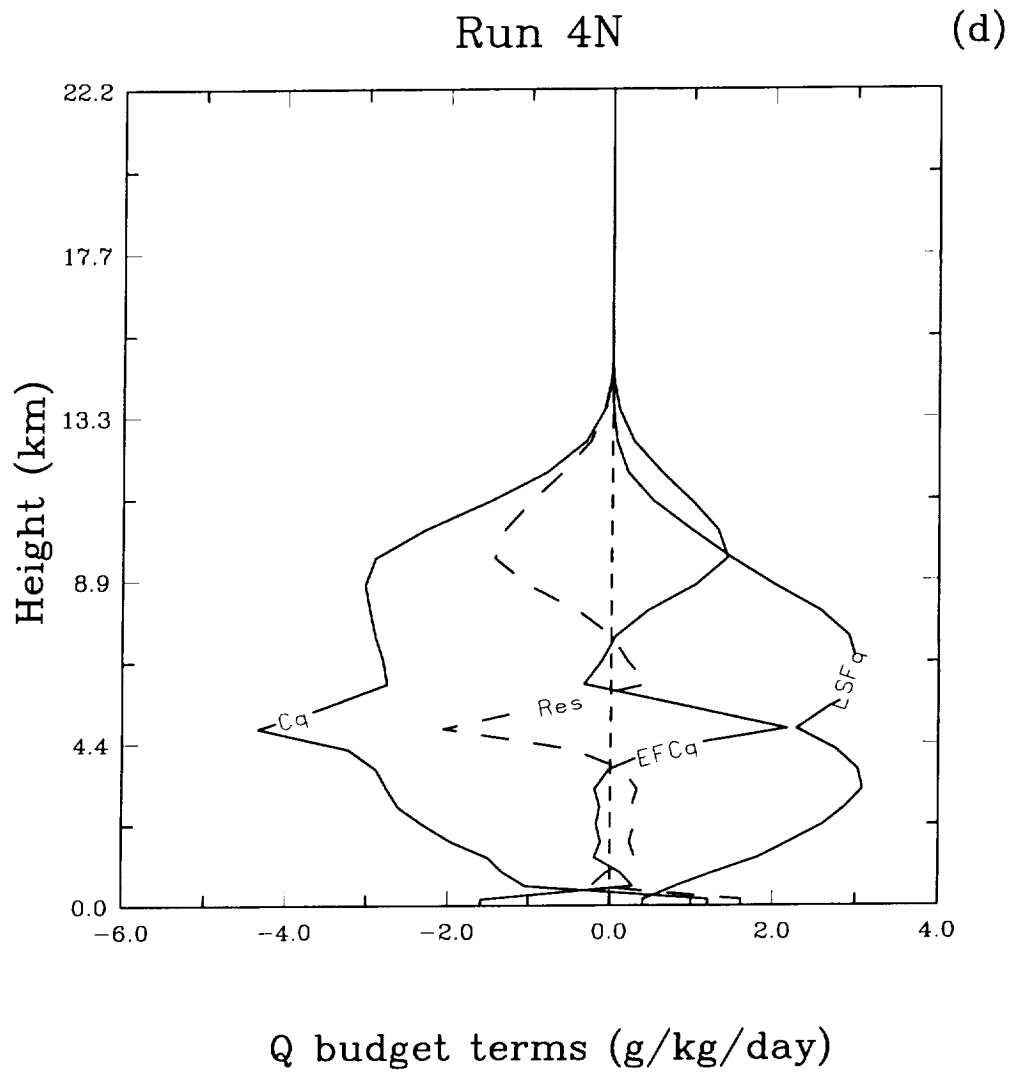


Fig. 9d

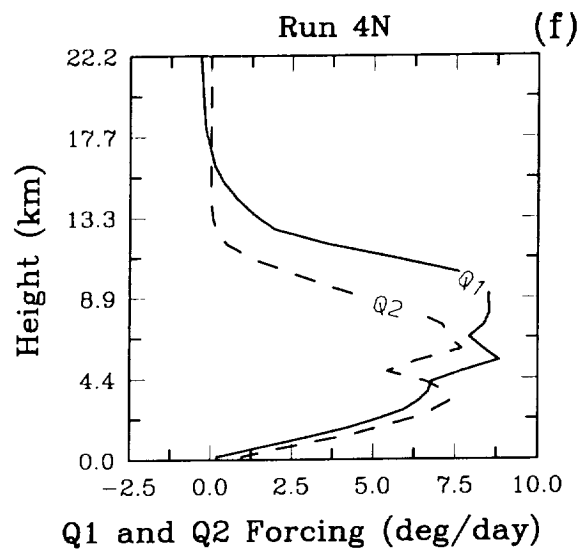
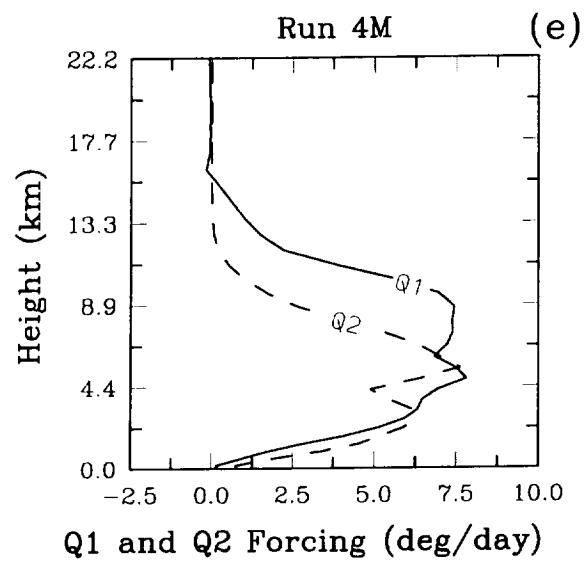


Fig. 9e, f

(a)

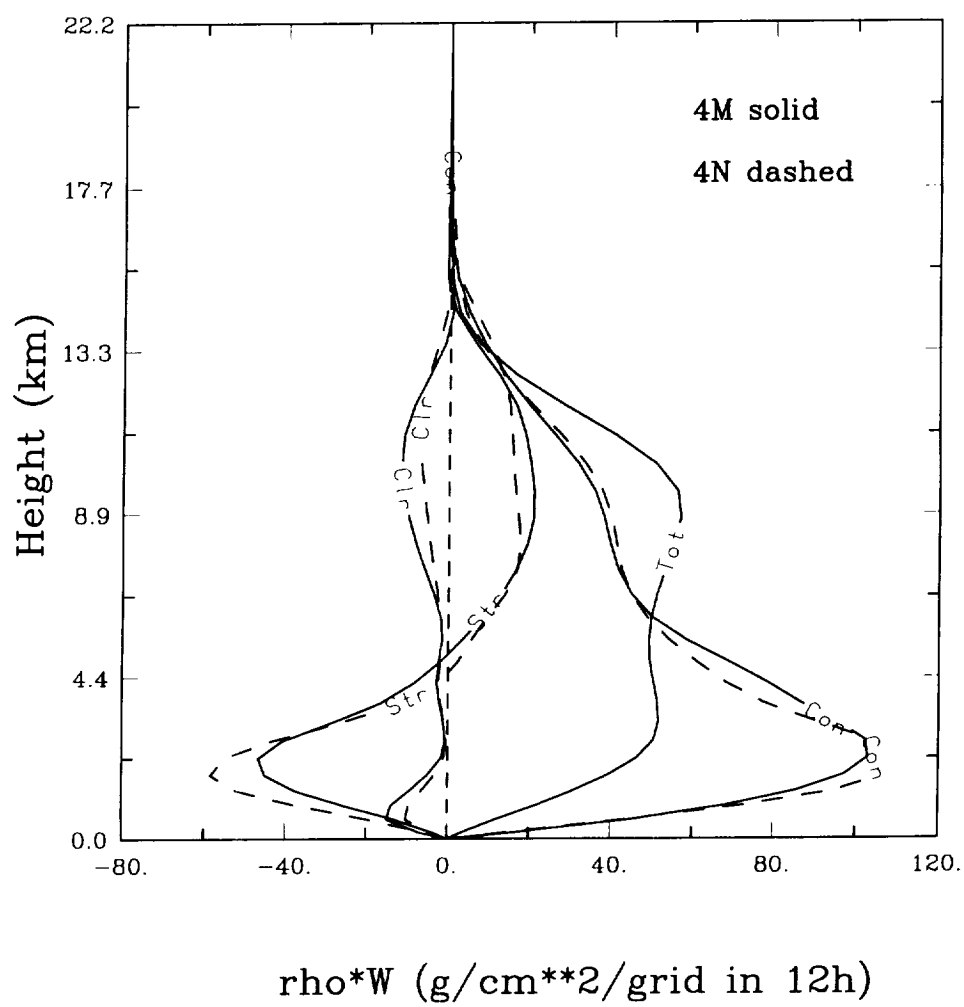


Fig. 10 a

(b)

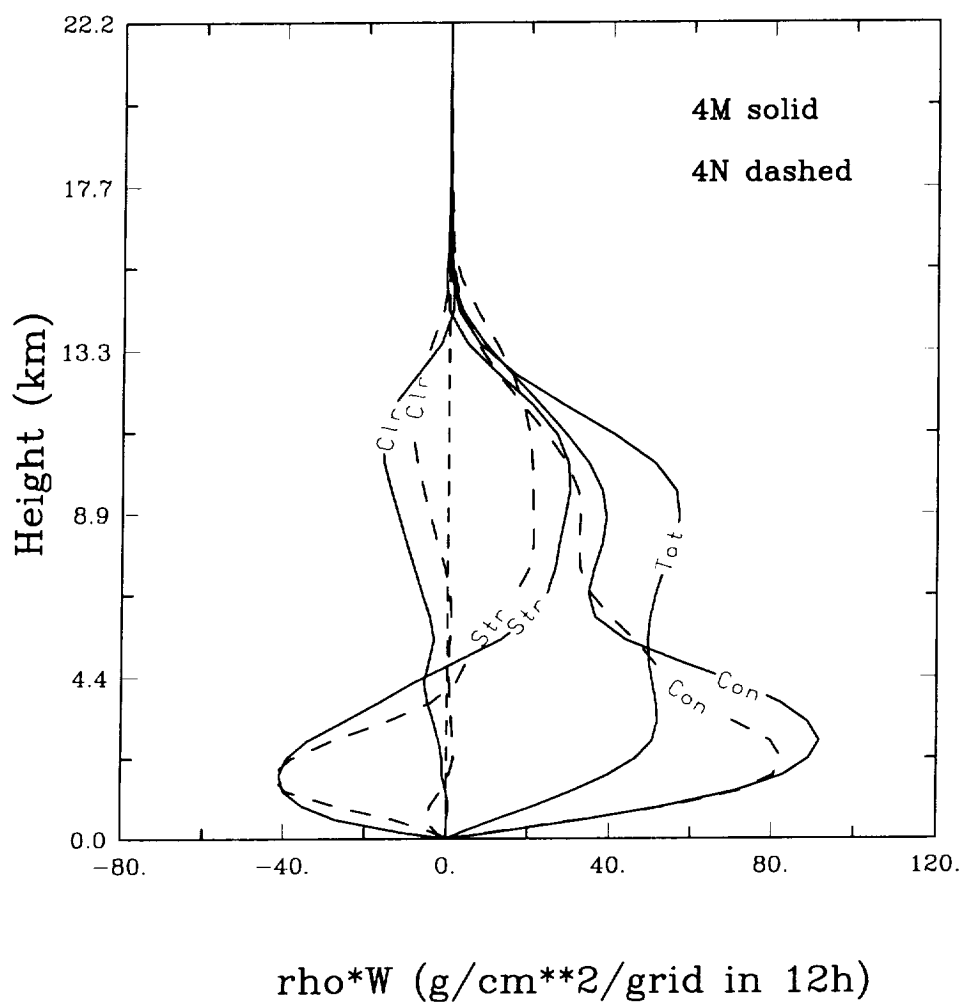


Fig. 10b

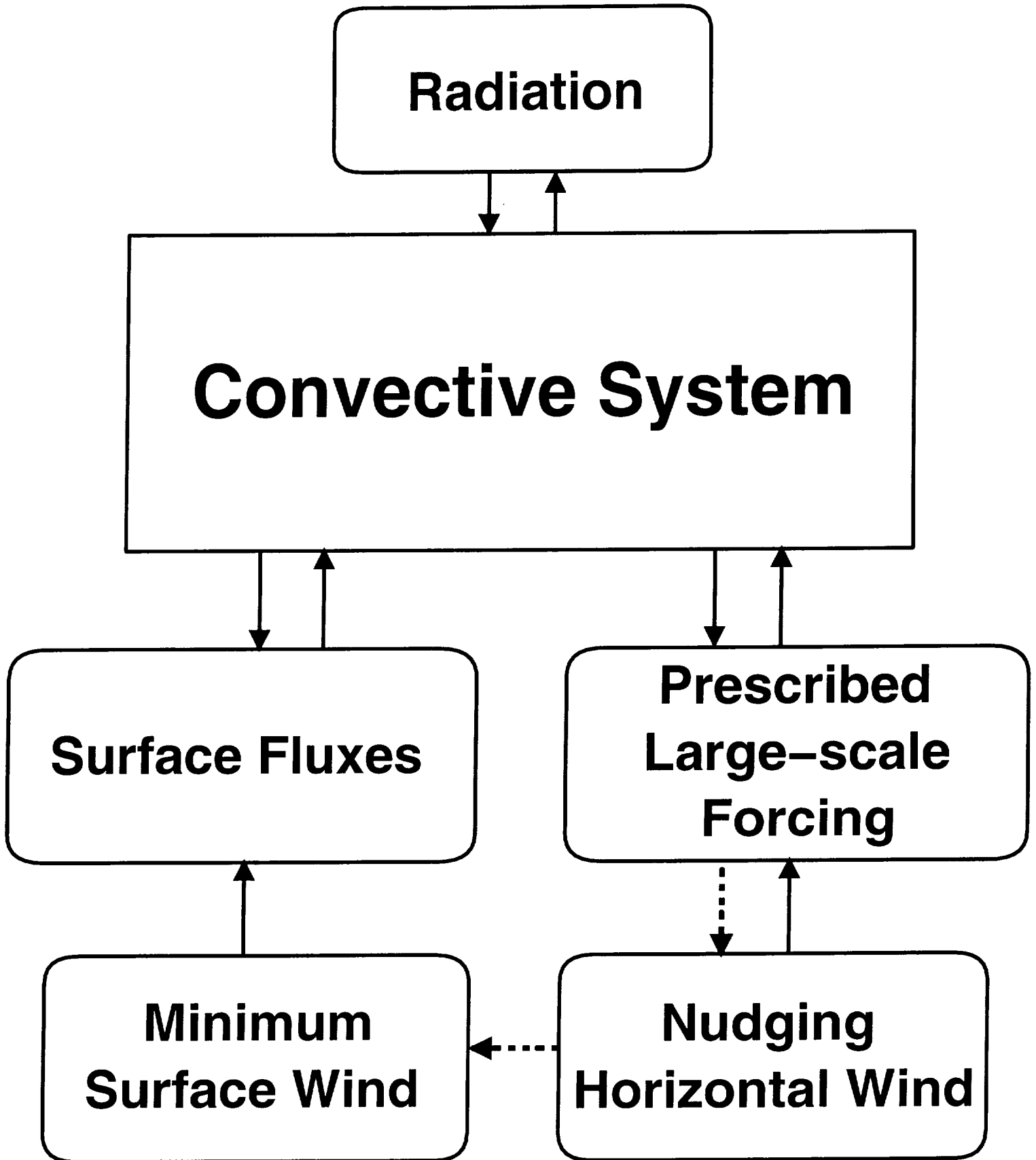


Fig. 11